

# Human aneuploid cells depend on the RAF/MEK/ERK pathway for overcoming increased DNA damage

---

Received: 12 June 2024

---

Accepted: 28 August 2024

---

Published online: 09 September 2024

---

 Check for updates

---


Johanna Zerbib<sup>1,13</sup>, Marica Rosaria Ippolito<sup>2,13</sup>, Yonatan Eliezer<sup>1</sup>, Giuseppina De Feudis<sup>2</sup>, Eli Reuveni<sup>1</sup>, Anouk Savir Kadmon<sup>1</sup>, Sara Martin<sup>2</sup>, Sonia Viganò<sup>2</sup>, Gil Leor<sup>1</sup>, James Berstler<sup>3</sup>, Julia Muenzner<sup>4</sup>, Michael Mülleder<sup>5</sup>, Emma M. Campagnolo<sup>6</sup>, Eldad D. Shulman<sup>6</sup>, Tiangen Chang<sup>6</sup>, Carmela Rubolino<sup>7</sup>, Kathrin Laue<sup>1</sup>, Yael Cohen-Sharir<sup>1</sup>, Simone Scorzoni<sup>2</sup>, Silvia Taglietti<sup>2</sup>, Alice Ratti<sup>2</sup>, Chani Stossel<sup>8,9</sup>, Talia Golan<sup>8,9</sup>, Francesco Nicassio<sup>7</sup>, Eytan Ruppin<sup>6</sup>, Markus Ralser<sup>4,10,11</sup>, Francisca Vazquez<sup>3</sup>, Uri Ben-David<sup>1,14</sup>  & Stefano Santaguida<sup>2,12,14</sup> 

Aneuploidy is a hallmark of human cancer, yet the molecular mechanisms to cope with aneuploidy-induced cellular stresses remain largely unknown. Here, we induce chromosome mis-segregation in non-transformed RPE1-hTERT cells and derive multiple stable clones with various degrees of aneuploidy. We perform a systematic genomic, transcriptomic and proteomic profiling of 6 isogenic clones, using whole-exome DNA, mRNA and miRNA sequencing, as well as proteomics. Concomitantly, we functionally interrogate their cellular vulnerabilities, using genome-wide CRISPR/Cas9 and large-scale drug screens. Aneuploid clones activate the DNA damage response and are more resistant to further DNA damage induction. Aneuploid cells also exhibit elevated RAF/MEK/ERK pathway activity and are more sensitive to clinically-relevant drugs targeting this pathway, and in particular to CRAF inhibition. Importantly, CRAF and MEK inhibition sensitize aneuploid cells to DNA damage-inducing chemotherapies and to PARP inhibitors. We validate these results in human cancer cell lines. Moreover, resistance of cancer patients to olaparib is associated with high levels of RAF/MEK/ERK signaling, specifically in highly-aneuploid tumors. Overall, our study provides a comprehensive resource for genetically-matched karyotypically-stable cells of various aneuploidy states, and reveals a therapeutically-relevant cellular dependency of aneuploid cells.

Aneuploidy, an imbalanced number of chromosomes, is a unique characteristic of cancer cells<sup>1–3</sup>. Whereas many of the effects of aneuploidy are chromosome-specific, the aneuploid state itself is associated with cellular stresses that aneuploid cells must overcome to survive and proliferate<sup>4,5</sup>. Uncovering the cellular coping mechanisms of aneuploid cells could enable their selective targeting.

So far, attempts to study aneuploidy in human cells have mostly focused on non-isogenic tumors<sup>6</sup> and cell lines<sup>7</sup>. For example, we have recently mapped the aneuploidy landscapes of ~1000 human cancer cell lines and revealed an increased vulnerability of aneuploid cancer cells to inhibition of the spindle assembly checkpoint and of the mitotic kinesin *KIF18A*<sup>7</sup>. However, such comparisons may be

---

A full list of affiliations appears at the end of the paper.  e-mail: [ubendavid@tauex.tau.ac.il](mailto:ubendavid@tauex.tau.ac.il); [Stefano.santaguida@ieo.it](mailto:Stefano.santaguida@ieo.it)

confounded by differences between non-isogenic cancer samples. Attempts to generate matched (pseudo-)diploid and aneuploid cell models have also been reported, mostly on p53-mutant and chromosomally unstable genetic backgrounds<sup>8,9</sup>. Karyotypically stable p53-WT models have been generated as well, but these models used microcell-mediated chromosome transfer that forced specific chromosomes upon the cells<sup>10,11</sup>, leading to massive chromosomal rearrangements<sup>12</sup>. To date, no study has systematically profiled the genomic, transcriptomic and functional landscapes of an isogenic aneuploid cell model. Therefore, a system of non-transformed, p53-WT isogenic cells that evolved aneuploidy through chromosome mis-segregation followed by natural selection, could be of high value.

A major consequence of aneuploidy is genomic instability. Aneuploidy has been associated with increased levels of DNA damage<sup>13</sup>: chromosome segregation errors promote genomic instability via several mechanisms, and aneuploidy itself can lead to perturbed DNA replication, DNA repair and mitosis<sup>14–21</sup>. This association is bi-directional, as replication stress can trigger structural and numerical chromosomal instability (CIN), resulting in aneuploidy<sup>22</sup>. Interestingly, aneuploid cancer cells have been shown to be resistant to DNA damage-inducing agents<sup>7,23–26</sup>, and this increased resistance has been linked to their overall drug resistance<sup>7,24</sup>, to their delayed cell cycle<sup>26</sup>, or to specific protective karyotype alterations<sup>23,25</sup>. Whether the ongoing genomic instability of aneuploid cells leads to elevated DNA damage repair (DDR) activity that could protect them from further induction of DNA damage, has remained an open question. In addition, it is currently unknown whether specific signaling pathways are activated in aneuploid cells in response to the elevated DNA damage, and whether such pathways might present a therapeutic opportunity.

Here, we establish a library of stable RPE1 clones with various degrees of aneuploidy. We perform systematic genomic and functional characterizations of 7 of these isogenic clones and reveal increased vulnerability of aneuploid cells to RAF/MEK/ERK pathway inhibition, and specifically to CRAF perturbation, which could also sensitize cells to DNA damage-inducing chemotherapies and to PARP inhibition. This aneuploidy-induced functional dependency is validated in human cancer cell lines and in patient-derived xenograft (PDX) models and may therefore be important for the development of cancer therapeutics, as well as for improved application of existing anticancer drugs.

## Results

### A model system to dissect the cellular consequences of aneuploidy

To identify pathways that are critical for the survival of aneuploid cells, we generated a system of isogenic aneuploid cell lines (and matching pseudo-diploid counterparts) derived from the untransformed, pseudo-diploid, immortalized retinal pigment epithelial cell line RPE1-hTERT (henceforth RPE1). This library was generated by transiently treating RPE1 with reversine, an MPS1 inhibitor, followed by single-cell sorting and clonal expansion<sup>17,27,28</sup> (Fig. 1a; Methods). Out of an initial pool of ~5000 single-cell sorted cells, ~200 clones (4%) were able to proliferate. Shallow whole-genome sequencing revealed 79 clones (~40%; Fig. 1b and Supplementary Data 1) with one or more aneuploid chromosome(s), on top of the gains of chromosome 10q and chromosome 12, which pre-exist in the parental RPE1 cells<sup>7,23</sup>.

About 60% of the aneuploid clones in our library displayed single chromosome aneuploidies. The vast majority of them (48 out of 50, 96%) harbored trisomies, and ~40% carried multiple aneuploidies (Fig. 1b, Supplementary Fig. 1a and Supplementary Data 1). Nearly all chromosomes were aneuploid in <15% of the clones, except for chromosome 11 that was aneuploid in ~25% of the clones (Fig. 1c). ~40% of chromosomes were completely absent from the library of single aneuploidies (chromosomes 1, 4, 6, 13, 16, 17, 19, 20 and 22; Fig. 1c), but

most of them were gained in clones harboring multiple aneuploidies (with the exception of chromosomes 1, 6 and 16; Fig. 1c). Importantly, whole-chromosome aneuploidies were much more common than segmental aneuploidies (90% vs. ~10% of clones, respectively; Supplementary Fig. 1b), in line with the known effects of whole-chromosome mis-segregation induced by MPS1 inhibition<sup>17,27,28</sup>, and with previous reports that structural aneuploidies could be tolerated only in *TP53*-deficient cells<sup>29</sup>.

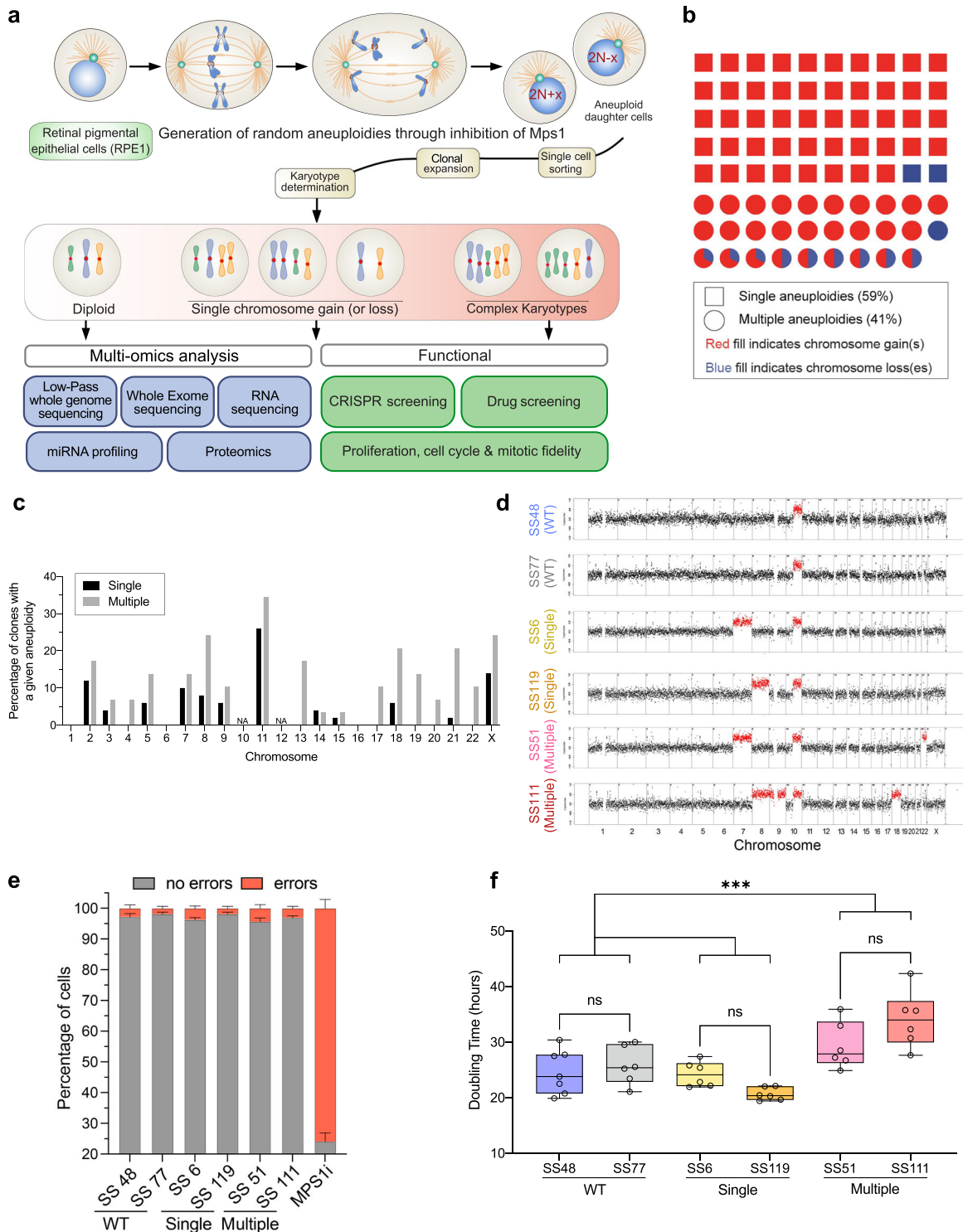
Although our library is not large enough to enable statistical analyses of specific chromosome patterns, our data suggest that the absence of certain chromosomes is likely due to selection, rather than skewed chromosome mis-segregation. Single-cell whole-genome sequencing (scWGS) of parental RPE1 cells<sup>30</sup> immediately following reversine exposure revealed only a mild aneuploidy recurrence bias that was highly similar to those recently reported<sup>31</sup> (higher-than-average aneuploidy rates for chromosomes 1–5, 8, 11 and X; lower-than-average rates for chromosomes 14, 15 and 19–22; Supplementary Fig. 1c). However, these mild biases could not explain the chromosome composition observed in our eventual library (with 9 chromosomes not appearing at all as single trisomies). Moreover, the relative aneuploidy prevalence of each chromosome immediately after treatment was not significantly correlated with its library representation. Overall, our analysis shows that randomly generated aneuploidies tend to be detrimental, with single monosomies being less tolerated than trisomies, and with some karyotypes being less fit than others, likely due to selection towards fitter clones.

### Proliferation, mitosis and cell cycle of the RPE1 clones

Next, we focused on aneuploid clones either trisomic for a given chromosome or harboring a complex karyotype in which the same chromosome gain was present in combination with other karyotypic alterations. We selected six clones for further characterization: two pseudo-diploid control clones, RPE1-SS48 and RPE1-SS77 (henceforth SS48 and SS77); two clones with single chromosome gains, RPE1-SS6 and RPE1-SS19 (henceforth SS6 and SS19), trisomic for chromosomes 7 and 8, respectively; and two clones with complex karyotypes, RPE1-SS51 that is trisomic for chromosomes 7 and 22, and RPE1-SS111 that is trisomic for chromosomes 8, 9 and 18 (henceforth SS51 and SS111) (Fig. 1d; note that gain of the q-arm of chromosome 10 is a clonal event in RPE1 cells).

As aneuploidy can often lead to chromosomal instability<sup>16,17,19,21,23,25</sup>, we next evaluated the fidelity of chromosome segregation by live-cell imaging (Supplementary Fig. 1d), quantifying mitotic errors, such as lagging chromosomes, anaphase bridges and micronuclei formation. Both WT and aneuploid clones displayed the same basal level of segregation defects (~2–5%; Fig. 1e and Supplementary Fig. 1e) and did not show significant differences in mitotic timing (Supplementary Fig. 1f). In contrast, reversine treatment led to chromosome segregation errors and shortened mitotic timing (Fig. 1e and Supplementary Fig. 1d–f; in agreement with previous reports<sup>17,27,28</sup>). Low-pass WGS (lp-WGS) following ten passages in culture confirmed the stable chromosomal composition of the clones (Supplementary Fig. 1g). Therefore, the stability of the aneuploid karyotypes should allow us to assess the cellular consequences of aneuploidy per se.

Aneuploidy has a detrimental effect on cell cycle progression<sup>7,11,17,28,32–34</sup>. A comparison of the pseudo-diploid and aneuploid clones demonstrated that the proliferation rate of clones harboring single trisomies was similar to that of pseudo-diploid clones, displaying a doubling time of roughly 24 h (Fig. 1f). Clones with complex karyotypes displayed a longer population doubling time (29 h for SS51 and 34 h for SS111; Fig. 1f and Supplementary Fig. 1h). Cell cycle analysis revealed that the increased doubling time of the highly-aneuploid clone was due to prolonged G2/M cell cycle phase (Supplementary Fig. 1i, j).



In sum, our efforts led to the generation of a library of matched non-transformed cells with various degrees of stable aneuploid karyotypes, providing a powerful tool for the genomic and functional characterization of the consequences of aneuploidy, and specifically of chromosome gains.

### Systematic genomic and functional characterization of the RPE1 clones

To characterize the genomics of our clones, we performed whole-exome sequencing (WES), and analyzed point mutations and copy number alterations (Methods). In line with RPE1 being a non-

transformed cell line, only a handful of cancer-relevant mutations were observed in the clones, the majority of which shared by all clones (Supplementary Fig. 2a and Supplementary Data 2). Surprisingly, however, the analysis revealed that SS77, one of the near-diploid control clones, acquired a clonal heterozygous p53-inactivating mutation (Supplementary Fig. 2a, b). WES-based copy number analysis confirmed the karyotypes of the clones (Supplementary Data 3). The highly-aneuploid clones carried many more focal copy number alterations (CNAs), compared to the pseudo-diploid clone and to the single-trisomy clones (Fig. 2a), suggesting a higher degree of genomic instability in these clones. Consistent with the acquisition of a p53-

**Fig. 1 | Characterization of matched aneuploid and pseudo-diploid clones.** **a** Schematic representation of clone generation. See the main text for a detailed description. **b** Chart showing the percentage of clones harboring single and multiple aneuploidies. Each shape represents a clone, with 79 clones shown in total. Squares represent clones with single aneuploidies, and circles represent clones with multiple aneuploidies. Red and blue indicate chromosome gains and losses, respectively, and the proportion of each color within the circle represents the fraction of gains/losses out of the aneuploid chromosomes. Clones harboring aneuploidies for chromosomes 10q and 12 were excluded, as they are already abundant in the parental RPE1 population. The library is enriched in clones harboring trisomies over monosomies ( $****p = 3.6 \times 10^{-7}$ , two-sided Chi-square test), and monosomies are more tolerated in multiple aneuploidies background than in single aneuploidy background ( $**p = 0.0024$ , two-sided Chi-square test). **c** Quantification of the percentage of clones harboring a given aneuploid chromosome in single (black) and multiple (gray) aneuploid clones. Chromosomes 10

and 12 were excluded, as a high fraction of the parental RPE1 cells already harbor a gain of one or both of these chromosomes. NA: not applicable. **d** Low-pass whole-genome sequencing (lp-WGS) copy number profiles, showing the karyotypes of selected pseudo-diploid (SS48 and SS77) and aneuploid (SS6, SS119, SS51, SS111) clones derived from RPE1 cells. Chromosome gains are colored in red, including the clonal gain of the q-arm of chromosome 10. Resulting karyotype is indicated in brackets. **e** Quantification of chromosome segregation errors (including lagging chromosomes, micronuclei, and anaphase bridges) determined by live-cell imaging. Treatment with the MPS1 inhibitor, reversine, was used as positive control.  $n = 4$  independent experiments. Graph shows the average  $\pm$  SEM. **f** Doubling time of pseudo-diploid (SS48 and SS77) and aneuploid (SS6, SS119, SS51, SS111) clones.  $n = 7$  (SS48) and  $n = 6$  (SS77, SS6, SS119, SS51, SS111) independent experiments. n.s.,  $p > 0.25$ ;  $***p = 0.0005$ ; One-way ANOVA, Tukey's multiple comparison test. Source data are provided as a Source Data file.

inactivating mutation, the number of CNAs in the SS77 clone was comparable to that in the highly-aneuploid clones (Supplementary Fig. 2c). These results suggested that SS77 should not be used as a pseudo-diploid clone but could be used instead as a p53-deficient clone.

We continued with comprehensive molecular characterization of the clones by investigating their gene expression profiles using RNA sequencing (RNAseq) and miRNA profiling, and their proteomes using mass-spectrometry-based proteomics. A principal component analysis (PCA) of each of these datasets showed that the highly-aneuploid clones, SS51 and SS111, clustered together despite harboring a completely different set of trisomies (Supplementary Fig. 2d–f). miRNAs that are transcriptionally activated by p53<sup>35–37</sup> (i.e. miR-34 family) were specifically downregulated in clone SS77 (Supplementary Fig. 2g), in line with the genetic inactivation of p53. Next, we performed a differential gene expression analysis, followed by pre-ranked gene set enrichment analysis (GSEA<sup>38,39</sup>), to identify gene expression signatures induced by aneuploidy regardless of the specific affected chromosome(s) (Supplementary Data 4–7). As expected, the over-expressed genes in each aneuploid clone were enriched for the gained chromosome(s) in both the RNAseq, miRNA-seq and proteomics datasets (Supplementary Fig. 2h–j). Importantly, however, chromosome-independent transcriptional signatures could also be identified. Both RNAseq and proteomics analysis revealed the significant upregulation of signatures related to DNA damage response and repair (DDR) (Fig. 2b, c and Supplementary Fig. 3a), suggesting that the aneuploid cells indeed cope with elevated levels of DNA damage. The aneuploid clones also significantly upregulated signatures related to RNA metabolism and pathways associated with management of proteotoxic stress (Supplementary Data 4–7), suggesting altered gene expression processes in the aneuploid clones, as detailed in our companion study<sup>40</sup>. On the other hand, aneuploid clones significantly downregulated transcriptional signatures associated with mitosis (Fig. 2b), in line with their slower proliferation rates (Fig. 1f), as well as transcriptional and proteomic signatures associated with drug metabolism (Fig. 2b, c).

Next, we performed a functional characterization of the sensitivity of the isogenic clones to genetic and pharmacological perturbations. We first performed genome-wide CRISPR/Cas9 screens in the 6 clones, and calculated the gene dependency scores for 18,120 genes (Methods; clone SS111 failed quality control and was therefore excluded from downstream analyses). We then compared the genetic dependencies between the aneuploid clones and the pseudo-diploid SS48 clone, using pre-ranked GSEA, to identify pathways that are preferentially essential either in pseudo-diploid or in aneuploid clones (Supplementary Data 8). Interestingly, the aneuploid clones were less sensitive than the pseudo-diploid clone to knockout of genes related to DNA damage response (Fig. 2d), suggesting that their adaptation to elevated levels of DNA damage enables them to cope better with further

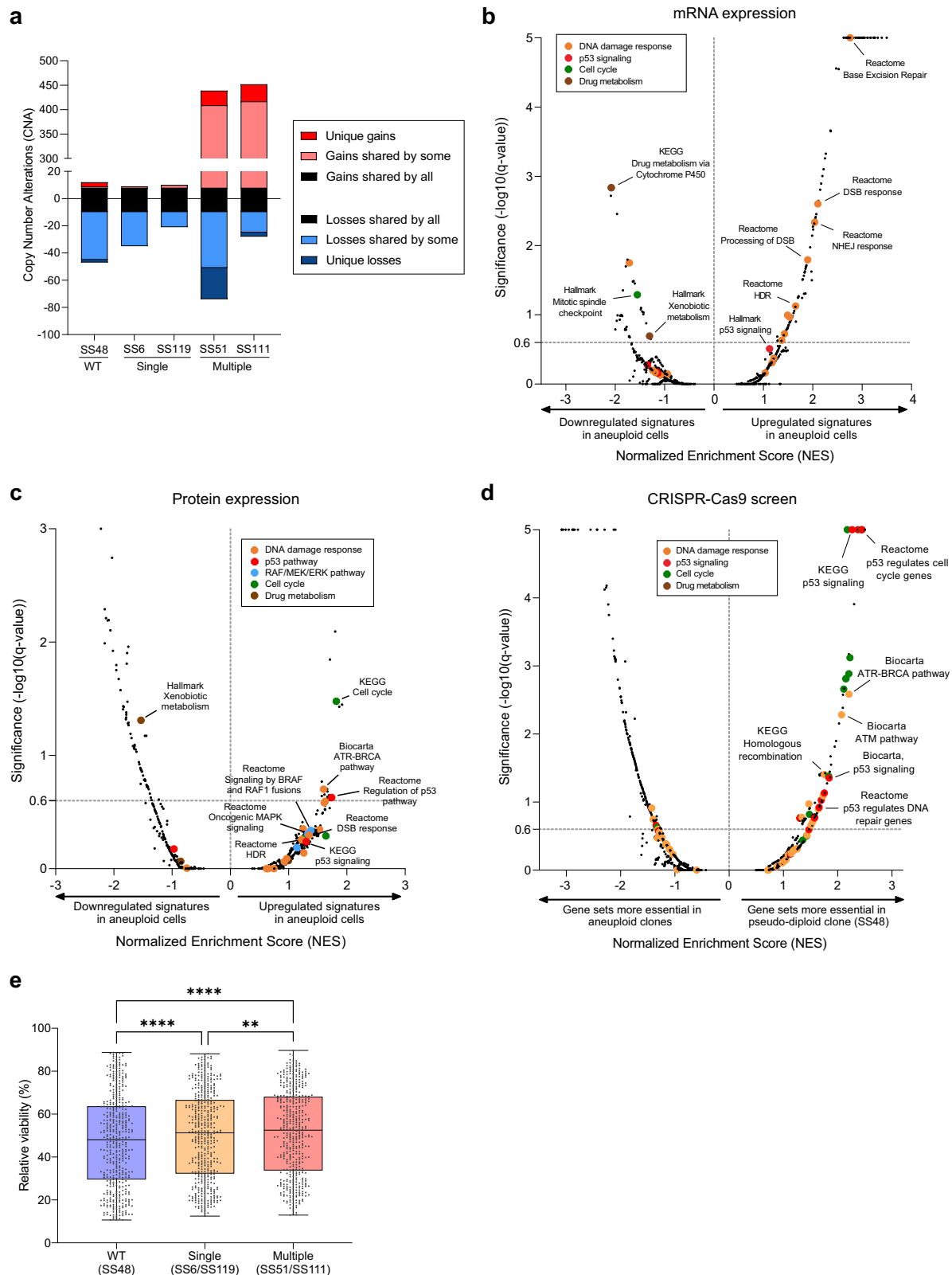
DNA damage induction. Of note, the aneuploid clones were also less sensitive to knockout of genes associated with cell cycle progression/regulation (Fig. 2d), in line with their slower proliferation rates (Fig. 1f). In addition, blocking p53 activity promoted cell proliferation to a greater extent in the aneuploid clones, reflected in our analysis as a decreased 'sensitivity' of the aneuploid clones to p53 pathway perturbation (Fig. 2d), suggesting an elevated basal activity of the p53 pathway in the aneuploid clones. Aneuploid cells were also more dependent on mechanisms related to RNA and protein metabolism (Supplementary Data 8), and we followed up on these findings in a companion study<sup>40</sup>.

Finally, we performed a pharmacological screen of 5336 small molecules, using the Broad Drug Repurposing Library<sup>41</sup> of drugs with known mechanisms of action. Each clone was exposed to 2.5  $\mu$ M of each compound in duplicates, and cell viability was assessed after 72 h (Methods; Supplementary Data 9). Interestingly, aneuploid clones were significantly more resistant to drug treatment in general, compared to the pseudo-diploid clone SS48 (Fig. 2e), consistent with the observed downregulation of drug metabolism in RNAseq and proteomics datasets (Fig. 2b, c). The more aneuploid the cells, the more resistant they were to drug treatments, in line with reports linking increased aneuploidy with reduced drug sensitivity<sup>7,24,26</sup>. Importantly, aneuploid cells were also more sensitive to specific classes of drugs (as detailed in the next sections). Notably, the differential vulnerabilities identified in the genetic and pharmacological screens were recapitulated when the p53-mutated, yet chromosomally unaltered, pseudo-diploid clone SS77 was included in the analysis (Supplementary Fig. 3b, c), further highlighting aneuploidy as the culprit of these differences.

Since aneuploid cancer cells are known to experience DNA damage<sup>13,14</sup> and exhibit increased resistance to cell cycle inhibitors<sup>26</sup>, DNA damage inducers<sup>7,23,25</sup>, and drugs in general<sup>7</sup>, we conclude that our isogenic non-transformed cell line models capture cancer-relevant aneuploidy-induced effects. We decided to focus our downstream validation and mechanistic studies on DDR (the current study) and RNA and protein metabolism<sup>40</sup>. We replaced the TP53-mutant SS77 clone with another TP53-WT pseudo-diploid clone, RPE1-SS31 (henceforth SS31), for validation studies, after confirming that its karyotype, proliferation rate and cell cycle profile were comparable to those of SS48 (Supplementary Fig. 4).

### Elevated DDR and increased resistance of aneuploid cells to DNA damage induction

Highly-aneuploid clones exhibited elevated transcriptional signatures of multiple DNA damage and repair gene sets (Fig. 3a and Supplementary Fig. 5a). To assess DNA damage we quantified the DNA damage markers 53BP1 and  $\gamma$ H2AX by immunofluorescence, focusing on EdU-negative cells to exclude replication-induced DNA damage. The number of positive nuclei was significantly higher in the highly-



aneuploid clones (Fig. 3b, c), consistent with the increased CNA prevalence in these cells (Fig. 2a). Interestingly, clones with a single trisomy exhibited an intermediate degree of DNA damage (Fig. 3b, c).

As aneuploid clones were less sensitive than the pseudo-diploid clone to knockout of genes related to DDR (Fig. 2d), we next focused on these genes, which included genes crucial for the response to both single-strand breaks (SSBs) and double-strand breaks (DSBs), such as

*RAD51*, *CHEK2*, *ATM*, *ATR*, *BRCA2*, and the *MRE11-NBN* complex<sup>42,43</sup> (Fig. 3d). This result suggests that the aneuploid clones are more resistant than the pseudo-diploid clones to further induction of DNA damage. We therefore compared their response to small molecules that directly induce DNA damage or interfere with DNA damage repair (42 compounds in our pharmacological screen). Indeed, aneuploid cells were significantly more resistant to these drugs, and drug

**Fig. 2 | Systematic genomic and functional characterization of RPE1 clones.** **a** Copy number alterations (CNAs) across the RPE1 clones. Highly-aneuploid clones, SS51 and SS111, exhibited the highest number of CNAs. **b** Preranked GSEA of the differential gene expression patterns (RNA-sequencing) between the pseudo-diploid SS48 clone (control) and the highly-aneuploid SS51 and SS111 clones. Plot presents enrichments for the Hallmark, KEGG, Biocarta and Reactome gene sets. Significance threshold set at  $q$ -value = 0.25. Enriched pathways are color-coded. **c** GSEA of the differential protein expression patterns (proteomics) between the pseudo-diploid clones SS48 and SS31 (controls) and highly-aneuploid SS51 and SS111 clones. Plot presents enrichments for Hallmark, KEGG, Biocarta and Reactome gene sets. Significance threshold set at  $q$ -value = 0.25. Enriched pathways are color-coded. **d** Preranked GSEA of the differential gene dependency scores

(genome-wide CRISPR screen) between the pseudo-diploid SS48 clone (control) and the aneuploid SS6, SS119 and SS51 clones. Plot presents enrichments for the Hallmark, KEGG, Biocarta and Reactome gene sets. Significance threshold set at  $q$ -value = 0.25. Enriched pathways are color-coded. **e** Comparison of overall drug sensitivity between a near-diploid control clone (SS48), clones with a single trisomy (SS6 and SS119), and clones with multiple trisomies (RPE1-SS51 and RPE1-SS111). Only drugs that led to a viability reduction ranging from -10% to -90% compared to DMSO control (see Methods) were considered.  $n = 456$  drugs.  $**p = 0.004$ ,  $****p = 2.3 \times 10^{-6}$  and  $p = 1.2 \times 10^{-8}$  for WT/Single and WT/Multiple, respectively; Repeated-Measures One-way ANOVA, Tukey's multiple comparison test. Source data are provided as a Source Data file.

resistance was correlated with the degree of aneuploidy (Fig. 3e), consistent with the observed levels of DNA damage (Fig. 3b, c). To validate these results, we treated aneuploid clones with two clinically relevant chemotherapies—the DSB-inducing etoposide and the SSB-inducing topotecan—and with the PARP inhibitor olaparib. The highly-aneuploid clones were significantly more resistant to these drugs compared to pseudo-diploid clones (Fig. 3f and Supplementary Fig. 5b–c), and the single trisomy clones displayed an intermediate phenotype (Fig. 3f).

*TP53* came up as the most differentially essential gene in the pseudo-diploid clones (Fig. 3d), likely due to activation of the p53 pathway in the aneuploid clones, which results in a greater proliferation boost upon p53 inhibition. Indeed, we found a significant up-regulation of p53 targets in the aneuploid clones (Supplementary Fig. 5d, e), consistent with the increased DNA damage observed in these clones. Western blot confirmed elevated levels of the p53 and p21 proteins in the highly-aneuploid clones (Fig. 3g, h). Moreover, qRT-PCR analysis of transcriptional downstream targets of p53 identified increased expression of several p53 targets, including those specifically linked to the DDR, such as *GADD45A*<sup>44</sup> (Fig. 3i and Supplementary Fig. 5f, g). Finally, we treated the RPE1 clones with the p53-activating compound nutlin-3a, and found that the highly-aneuploid clones were significantly more resistant to p53 activation than the pseudo-diploid clones (Fig. 3j). Together, these findings suggest that the aneuploid clones experience higher DNA damage levels, leading to p53 pathway activation and increased DDR, which render them less sensitive to further induction of DNA damage (as well as to further p53 activation).

To assess the generalizability of these findings, we turned to a second isogenic system of RPE1 cells and their aneuploid derivatives, RPTs<sup>8</sup>. In this system, inhibition of cytokinesis led to tetraploidization of the RPE1 cells, resulting in chromosomal instability that soon made them highly-aneuploid<sup>8</sup>.  $\gamma$ H2AX staining revealed significantly more ongoing DNA damage in the aneuploid RPT cells in comparison to their pseudo-diploid parental cells (Supplementary Fig. 5h, i). Moreover, the RPT cells were more resistant to both etoposide and topotecan, and their resistance patterns matched their pre-existing DNA damage levels (Supplementary Fig. 5j, k). Furthermore, reversine-induced aneuploidization in two additional non-transformed (BJ-hTERT and IMR90) and two additional cancer (CAL51 and SW48) cell lines increased the cellular resistance to etoposide (Supplementary Fig. 5l, m). Therefore, increased DNA damage and subsequent resistance to DNA damage induction characterize aneuploid cells across cell lines and aneuploidy induction methods.

Lastly, we addressed whether these findings also apply to aneuploid human cancer cells in general. We extended our published table of aneuploidy scores of human cancer cell lines<sup>7</sup> to 1742 cell lines (Supplementary Data 10; Methods). Matched doubling times were available for ~500 of these cancer cell lines<sup>45</sup>, allowing us to investigate whether elevated DDR is required for the proliferation of aneuploid cells. Indeed, the genes associated with the proliferation capacity of highly-aneuploid, but not of near-euploid, cell lines were enriched for DDR signatures (Fig. 3k, Supplementary Data 11, and Methods).

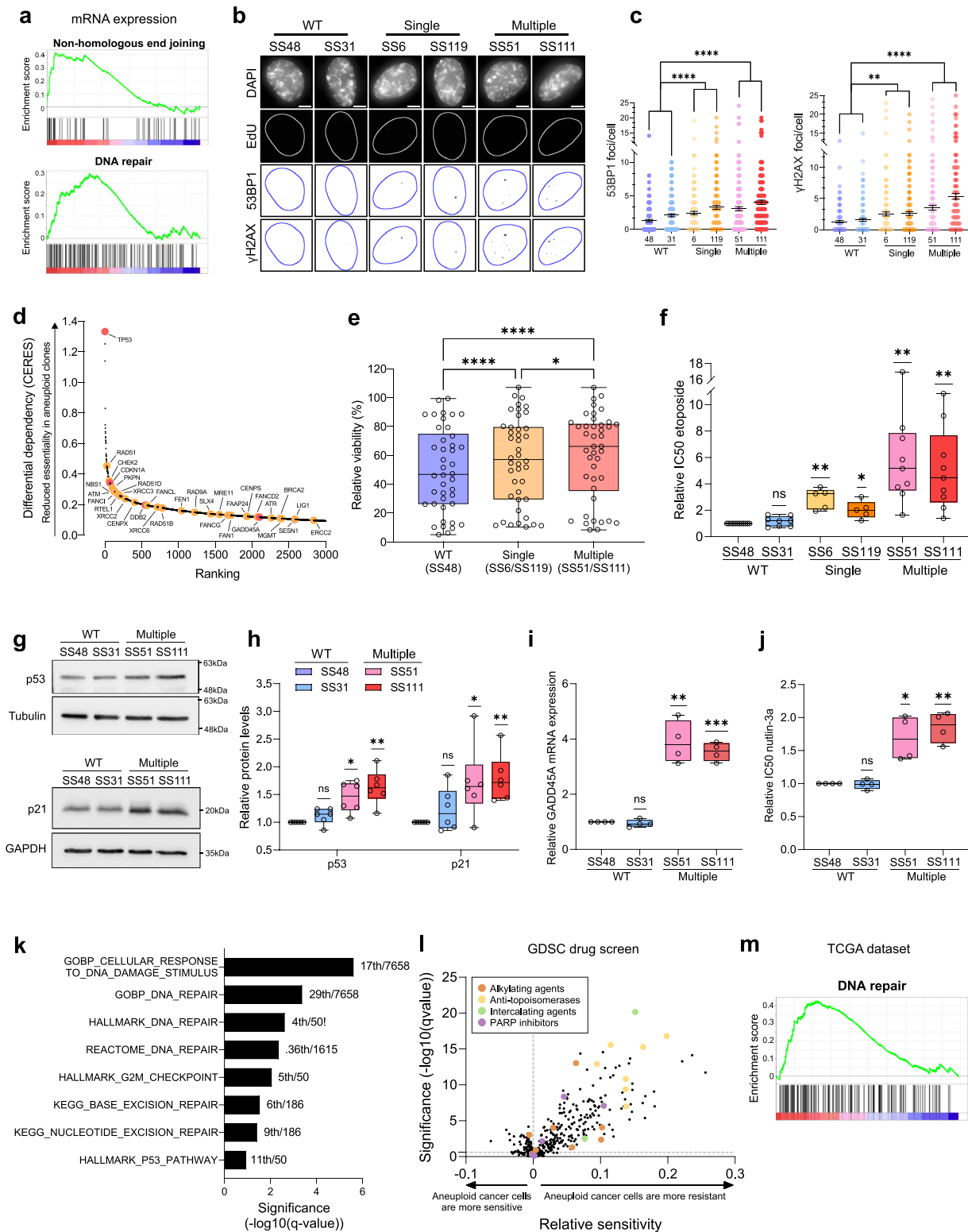
Moreover, aneuploid human cancer cells were significantly more resistant to chemical agents that directly induce DNA damage or perturb DNA damage repair across several independent drug screens<sup>46–49</sup> (Fig. 3l and Supplementary Fig. 5n, o), even when doubling time was controlled for (Supplementary Fig. 5p). Finally, a lineage-controlled pan-cancer analysis of The Cancer Genome Atlas (TCGA) showed a significant elevation of the *DDR* gene expression signature in highly-aneuploid human tumors (Fig. 3m and Supplementary Fig. 5q). We conclude that ongoing DNA damage, activated DDR, and increased resistance to DNA damage induction, are fundamental characteristics of both non-transformed and cancerous aneuploid cells.

### Increased CRAF activity and dependency in aneuploid cells

We next analyzed our pharmacological screen to identify increased vulnerabilities of the aneuploid clones. Although the aneuploid clones were generally more resistant to drug treatments (Fig. 2e), they were significantly more sensitive to RAF/MEK/ERK pathway inhibition (Fig. 4a). We validated the differential drug sensitivity to two of the top differentially-active RAF inhibitors, TAK632 and 8-Br-cAMP, and found that the highly-aneuploid clones were significantly more sensitive to both (Fig. 4b, c and Supplementary Fig. 6a, b), with the single-trisomy clone SS119 (but not SS6) exhibiting an intermediate phenotype (Supplementary Fig. 6c). Interestingly, TAK632 is a pan-RAF inhibitor exhibiting increased affinity for CRAF (also known as Raf-1) over BRAF<sup>50</sup>, and 8-Br-cAMP was previously described as a specific CRAF inhibitor<sup>51</sup>, suggesting a specific role for CRAF in the observed RAF dependency.

Several studies have pointed to a connection between RAF activity and aneuploidy induction<sup>52–55</sup>. Thus, we measured RAF activation in our clones, primarily focusing on CRAF as suggested by the drug response analysis. CRAF was consistently activated (as measured by pCRAF/CRAF protein ratio) in the highly-aneuploid clones (Fig. 4d, e), but not in the single-trisomy clones (Supplementary Fig. 6d, e), suggesting that CRAF activation in the highly-aneuploid clones underlies their increased sensitivity to RAF inhibitors. Indeed, CRAF knockdown using siRNAs (Supplementary Fig. 6f, g) had an inhibitory effect on the proliferation of highly-aneuploid clones, but not on pseudo-diploid clones (Fig. 4f, g and Supplementary Fig. 6h), and had an intermediate effect on the single-trisomy clones (Supplementary Fig. 6h). Next, we applied live-cell imaging to follow cellular response to 8-Br-cAMP (Supplementary Fig. 6i) and found that the effects of CRAF inhibition on cell proliferation (Supplementary Fig. 6j, k), cell morphology (Supplementary Fig. 6l, m), and cell motility (Supplementary Fig. 6n, o) were all significantly stronger in the highly-aneuploid clones. Finally, there was no significant difference in cell death between the pseudo-diploid and highly-aneuploid clones following CRAF inhibition (Supplementary Fig. 6p, q). We therefore conclude that highly-aneuploid clones preferentially depend on CRAF activity for their proliferation, and that CRAF inhibition is mostly cytostatic, rather than cytotoxic, for the aneuploid cells.

Previous studies have shown that CRAF activation follows BRAF/CRAF heterodimerization<sup>56,57</sup>. Thus, we treated the cells with PLX7904,



a RAF inhibitor developed to inhibit BRAF/CRAF heterodimerization and the resultant CRAF activation<sup>58–60</sup>. Consistent with the response to the other two RAF inhibitors, highly-aneuploid clones were more sensitive to PLX7904 compared to pseudo-diploid clones (Supplementary Fig. 7a). Therefore, we also investigated BRAF in our system. BRAF expression levels were consistently elevated only in SS51 (Supplementary Fig. 7b–d), which harbors an extra copy of chromosome 7 on which BRAF resides (BRAF is constitutively phosphorylated<sup>61</sup> so its activity cannot be assessed by measuring phosphorylation).

Consistent with the importance of BRAF/CRAF heterodimerization, highly-aneuploid clones (but not single-trisomy clones) were significantly more sensitive to BRAF knockdown than their diploid counterparts (Supplementary Fig. 7e, f). We conclude that both BRAF, CRAF and their interactions are important for the dependency to RAF inhibitors in highly aneuploid clones.

To assess whether CRAF activation is an immediate adaptation of cells following aneuploidy induction, we quantified its activity immediately after reversine treatment. We found increased CRAF activity

**Fig. 3 | Elevated DDR and increased resistance of aneuploid cells to DNA damage induction.** **a** GSEA of the Reactome ‘Non-Homologous End Joining’ (NES = 2.06,  $q$ -value = 0.0026) and Hallmark ‘DNA repair’ (NES = 1.72,  $q$ -value = 0.013) gene sets in highly-aneuploid clones, SS51 and SS111, vs. pseudo-diploid clone SS48. **b, c** Representative IF images (**b**) and quantification (**c**) of 53BP1 and  $\gamma$ H2AX foci in non-replicative (EdU-negative) cells across the RPE1 clones. Scale bar, 5  $\mu$ m. Data obtained from 3 independent experiments,  $n = 137$  (SS48), 146 (SS31), 157 (SS6), 157 (SS119), 156 (SS51), and 148 (SS111). \*\*\*\* $p = 3.7 \times 10^{-6}$  (pseudo-diploid/single clones) and  $p = 1.1 \times 10^{-10}$  (pseudo-diploid/multiple clones);  $\gamma$ H2AX: \*\* $p = 0.0015$  (pseudo-diploid/single clones), \*\*\* $p = 4 \times 10^{-15}$  (pseudo-diploid/multiple clones); Kruskal–Wallis test, Dunn’s multiple comparison. Bars, mean  $\pm$  SEM. **d** Top 3000 genes in genome-wide CRISPR/Cas9 screening of aneuploid clones vs. the pseudo-diploid clone SS48. Highlighted are key genes that belong to the p53 pathway (in red) or to DNA damage response (in orange). **e** Comparison of cellular sensitivity to drugs that directly induce DNA damage (alkylating and intercalating agents, anti-topoisomerases and PARP inhibitors) across the RPE1 clones. \* $p = 0.0482$ ; \*\*\*\* $p = 2.1 \times 10^{-6}$  and  $p = 4.3 \times 10^{-6}$  for pseudo-diploid/Single and pseudo-diploid/Multiple, respectively; Repeated-Measure One-Way ANOVA, Tukey’s multiple comparison test.  $n = 42$  drugs. **f** Drug sensitivity to 72 h treatment with etoposide across the RPE1 clones.  $n = 12$  (SS48),  $n = 8$  (SS31),  $n = 5$  (SS6, SS119) and  $n = 9$

(SS51, SS111) independent experiments. \* $p = 0.0252$  for SS119, \*\* $p = 0.0046$ ,  $p = 0.0081$  and  $p = 0.0046$ , for SS6, SS51 and SS111, respectively; two-sided one-sample  $t$ -test. **g** Western blot of p53 (top) and p21 (bottom) in pseudo-diploid clones and highly-aneuploid clones. **h** Protein expression of p53 and p21, relative to SS48.  $n = 6$  independent experiments. (p53) \* $p = 0.0104$  and \*\* $p = 0.0042$ , for SS51 and SS111, respectively; (p21) \* $p = 0.0431$  and \*\* $p = 0.0061$ , for SS51 and SS111, respectively; two-sided one-sample  $t$ -test. **i** mRNA expression of the p53 transcriptional target GADD45A, in pseudo-diploid and highly-aneuploid clones.  $n = 4$  independent experiments. \*\* $p = 0.0049$  (SS51); \*\*\* $p = 0.0006$  (SS111); two-sided one-sample  $t$ -test. **j** Drug sensitivity to 72 h treatment with nutlin-3a in pseudo-diploid vs. highly-aneuploid clones.  $n = 4$  independent experiments. \* $p = 0.0265$  (SS51); \*\* $p = 0.0052$  (SS111); two-sided One-Sample  $t$ -test. **k** GSEA of genes whose expression correlates with proliferation in highly-aneuploid but not in near-diploid cancer cell lines. The ranking of each DDR signature out of all signatures included in each collection is indicated. **l** Differential drug sensitivities between near-euploid and highly-aneuploid human cancer cell lines. Direct DNA damage inducers are highlighted in orange, green, yellow and purple. **m** GSEA of Hallmark ‘DNA repair’ signature in human primary tumors with high vs. low aneuploidy (NES = 1.73;  $q$ -value = 0.001). Source data are provided as a Source Data file.

following MPS1 inhibition in near-diploid RPE1 cells (Fig. 4h, i and Supplementary Fig. 8a, b). Aneuploidy induction using nocodazole and STLC wash-out also led to CRAF activation (Supplementary Fig. 8c, d). Importantly, the inhibitory effect of CRAF knockdown on cell proliferation significantly increased following reversine-induced aneuploidization (Fig. 4j and Supplementary Fig. 8e), confirming that aneuploidy increases the cellular sensitivity to CRAF inhibition. Elevated CRAF activity and increased vulnerability to CRAF inhibition were also recapitulated in the second isogenic system of RPE1 cells and their highly-aneuploid RPT derivatives (Supplementary Fig. 8f–i). Similarly, reversine-induced aneuploidization of the diploid cell lines, IMR90 and CAL51, also rendered them more sensitive to CRAF depletion (Supplementary Fig. 8j–k).

We then asked whether CRAF activity is associated with a high degree of aneuploidy in human cancer cells as well. Quantification of the pCRAF/CRAF protein ratio across 455 highly-aneuploid vs. near-euploid cancer cell lines<sup>62</sup>, revealed increased CRAF activity in highly-aneuploid cancer cells (Fig. 4k; BRAF and CRAF total protein levels were not changed<sup>63</sup> (Supplementary Fig. 8l, m)). Importantly, analysis of a large cohort of pediatric PDX models<sup>64</sup> revealed that highly-aneuploid tumors were significantly more sensitive to RAF inhibitors than lowly-aneuploid tumors (Fig. 4l). We conclude that aneuploid cancer cells activate CRAF as well.

Interestingly, CRAF activity is functionally linked to DDR<sup>65,66</sup>. Specifically, CRAF is activated in response to DNA damage, and its pharmacological or genetic inhibition sensitizes cells to ionizing radiation or genotoxic drugs<sup>65</sup>. Indeed, etoposide treatment in the parental RPE1 cells led to a significant increase in their CRAF activity (Fig. 4m, n). Moreover, CRAF activation correlated with resistance to etoposide, and to DNA damage-inducing drugs in general, across human cancer cell lines (Supplementary Fig. 8n, o). To investigate causality, we next treated the pseudo-diploid clone SS48 and the highly-aneuploid clones SS51 and SS111 with a sub-lethal dose of the CRAF inhibitor TAK632 for 72 h (Supplementary Fig. 8p), in combination with the DSB-inducing drug etoposide or with the PARP inhibitor olaparib. CRAF inhibition specifically sensitized the aneuploid cells to etoposide (Fig. 4o) and olaparib (Fig. 4p), confirming that CRAF activation was required to overcome DNA damage in the aneuploid clones.

### Increased MEK/ERK activity and dependency in aneuploid cells

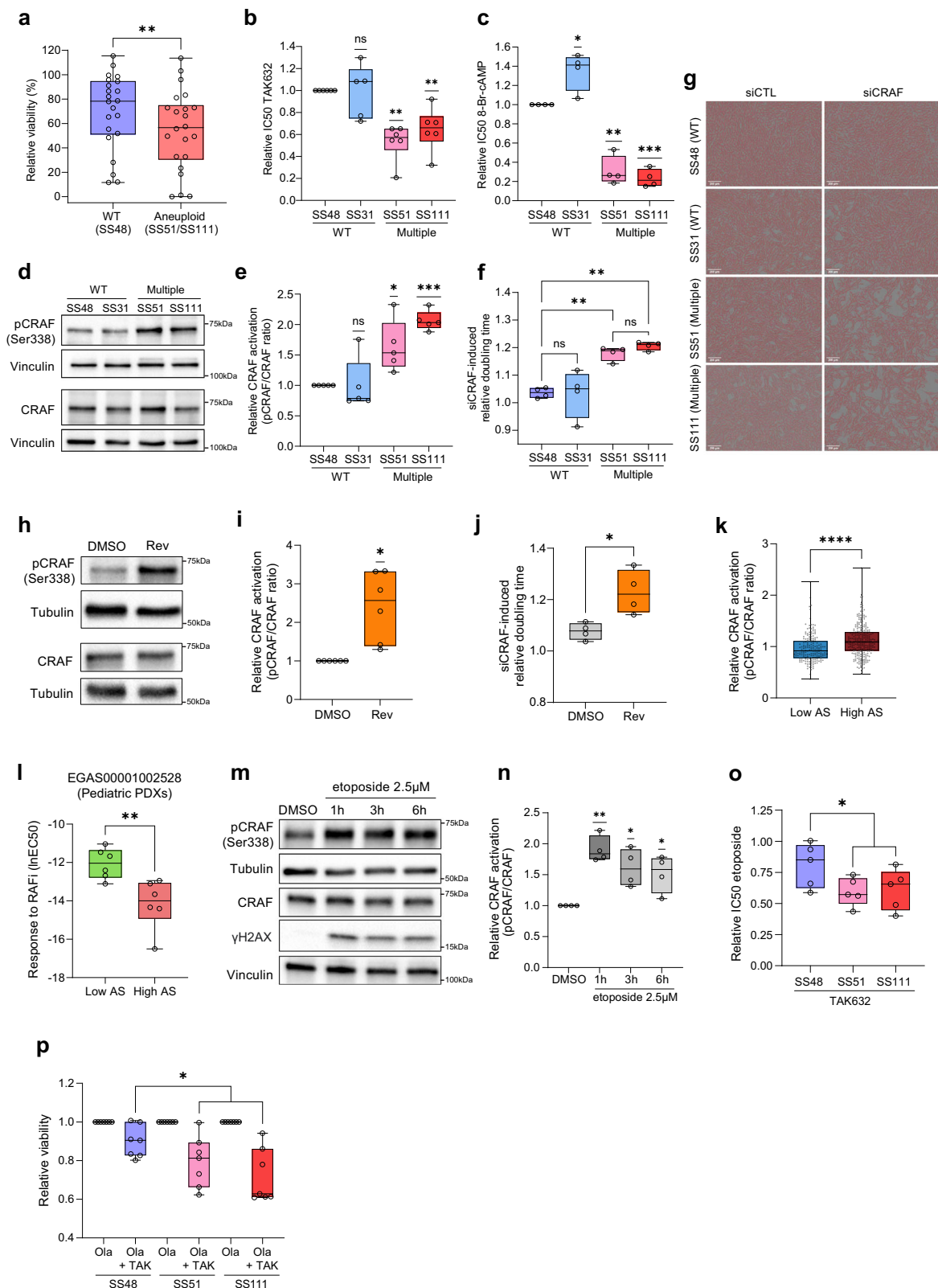
We next investigated the activation of the canonical CRAF downstream targets, MEK and ERK. Indeed, both MEK and ERK activity was significantly higher in the highly-aneuploid clones (but not in single-

trisomy clones) than in the pseudo-diploid ones (Fig. 5a–d and Supplementary Fig. 9a–d), indicating that the activity of the RAF/MEK/ERK signaling cascade is elevated in highly-aneuploid cells, in line with our proteomic analysis (Fig. 2c). We therefore compared the vulnerability of pseudo-diploid and aneuploid cells to MEK and ERK inhibition. The highly-aneuploid clones were significantly more sensitive to the clinically-approved MEK inhibitor, trametinib (Fig. 5e), and tended to be more sensitive to selumetinib as well (Supplementary Fig. 9e). Moreover, highly-aneuploid clones were significantly more sensitive to the ERK inhibitor, ulixertinib (Fig. 5f and Supplementary Fig. 9f). Aneuploid clones therefore depend on the entire RAF/MEK/ERK pathway. Importantly, MEK over-expression in parental RPE1 cells (Supplementary Fig. 9g) reduced their sensitivity to CRAF inhibition (Supplementary Fig. 9h), demonstrating that this sensitivity is mainly mediated by canonical MAPK signaling.

We next assessed whether MEK and ERK activation is an immediate response of cells to aneuploidy induction. Indeed, both MEK and ERK activities increased significantly following aneuploidy induction by reversine (Fig. 5g–j), nocodazole or STLC treatments (Supplementary Fig. 9i–l). We then examined whether MEK and ERK activities are also associated with aneuploidy in human cancer cells, and found an increased activity of both MEK and ERK in highly-aneuploid cancer cells<sup>62</sup> (Fig. 5k, l), consistent with the increased CRAF activity (Fig. 4k). We conclude that the increased activity of the RAF/MEK/ERK pathway is associated with a high degree of aneuploidy in cancer cells as well.

The sensitivity of aneuploid cells to MEK inhibitors is of particular importance given their clinical use. Aneuploid cancer cells were significantly more sensitive to MEK inhibitors (Fig. 5m and Supplementary Fig. 9m). Aneuploidy induction in two additional non-transformed (BJ-hTERT and IMR90) and two additional cancer (CAL51 and SW48) cell lines further demonstrated that aneuploidization increased the cellular sensitivity to MEK inhibition (Supplementary Fig. 9n–o). Next, we performed a pooled screen of cell lines, using the PRISM barcoded cell line platform<sup>47</sup>, assessing the response of 578 human cancer cell lines to selumetinib, in combination with a low dose (250 nM) of reversine or a vehicle-control (Methods). Whereas the proliferation effect of reversine itself at this low concentration was mild (Supplementary Data 12), it significantly sensitized the cancer cell lines to MEK inhibition (Fig. 5n). Furthermore, highly-aneuploid pediatric PDXs tended to be more sensitive to trametinib than lowly-aneuploid PDXs (albeit this was not statistically significant; Supplementary Fig. 9p). We thus conclude that highly-aneuploid cancer cells are more sensitive to MEK inhibition.





Several studies have documented a beneficial effect of combining MEK/ERK inhibitors with DDR inhibitors in multiple myeloma and pancreatic cancer<sup>67,68</sup>. Therefore, we asked whether the activation of the RAF/MEK/ERK pathway in aneuploid cells underlies their resistance to DNA damage induction. Indeed, MEK overexpression reduced the sensitivity of RPE1 cells to both etoposide (Fig. 5o) and olaparib (Supplementary Fig. 9q). Further, a sub-lethal dose of trametinib

(Supplementary Fig. 9r-s) significantly sensitized highly-aneuploid clones to etoposide (Fig. 5p). Consistently, ERK activation was associated with increased resistance to DNA damage-related drugs across hundreds of cancer cell lines (Supplementary Fig. 9t).

Finally, we analyzed genomic and drug response data from a couple of clinical cohorts: pancreatic PDXs treated with olaparib<sup>69</sup> and breast cancer patients treated with olaparib in combination with

**Fig. 4 | Aneuploid cells exhibit increased activity and dependency to CRAF, which is functionally linked to DNA damage repair.** **a** Sensitivity to RAF/MEK/ERK inhibitors ( $n = 22$  drugs) in a near-diploid control clone vs. highly-aneuploid clones.  $**p = 0.0018$ , two-tailed paired  $t$ -test. **b, c** Drug sensitivity to 72 hr treatment with the CRAF inhibitors TAK632 (**b**) and 8-Br-cAMP (**c**) in pseudo-diploid vs. highly-aneuploid clones. TAK632:  $n = 5$  (SS31) and  $n = 6$  (SS48, SS51, SS111) independent experiments;  $**p = 0.001$  (SS51);  $p = 0.007$  (SS111). 8-Br-cAMP:  $n = 4$  independent experiments;  $**p = 0.0017$  (SS51);  $***p = 0.002$  (SS111); two-sided one-sample  $t$ -test. **d** Western blot of pCRAF (Ser338) and total CRAF in pseudo-diploid and highly-aneuploid clones. **e** Quantification of CRAF activation (pCRAF/CRAF ratio).  $n = 5$  independent experiments.  $*p = 0.028$  (SS51);  $***p = 0.001$  (SS111); two-sided one-sample  $t$ -test. **f** Doubling time of the pseudo-diploid and highly-aneuploid clones following CRAF knockdown.  $n = 4$  independent experiments.  $**p = 0.0047$ ,  $p = 0.0012$ ,  $p = 0.0041$  and  $p = 0.0010$  for SS51/SS48, SS111/SS48, SS51/SS31, SS111/SS31 respectively; two-sided One Way ANOVA, Tukey's multiple comparison. **g** Representative images of CRAF knockdown. Ilastik cell masking shown in red. Scale bar, 200  $\mu$ m. **h** Western blot of pCRAF and total CRAF in reversine-pulsed RPE1 cells. **i** CRAF activation in the reversine-pulsed cells, relative to the DMSO control.  $n = 6$  independent experiments.  $*p = 0.0122$ ; two-sided One Sample  $t$ -test. **j** Doubling time following CRAF knockdown in aneuploidy-induced RPE1 cells.

Proliferation rate calculated relative to a control siRNA treatment.  $n = 4$  independent experiments;  $*p = 0.0157$ ; two-tailed unpaired  $t$ -test. **k** CRAF activity in the top and bottom aneuploidy quartiles of human cancer cell lines ( $n = 455$ ). Data obtained from DepMap 22Q1 release.  $****p = 6.5 \times 10^{-9}$ , two-tailed Mann-Whitney test.

**l** Comparison of the response (InEC50) of lowly and highly aneuploid pediatric PDXs<sup>64</sup> to RAF inhibitors. Dots represent the averages of the three tested drugs (LGX-818, vemurafenib, dabrafenib).  $n = 6$  PDX per group;  $**p = 0.0043$ , one-tailed Mann-Whitney  $t$ -test. **m** Western blot of pCRAF (Ser338), total CRAF, and  $\gamma$ H2AX in RPE1 cells treated with etoposide (2.5  $\mu$ M) for 1, 3 or 6 h. **n** CRAF activation in etoposide-treated cells, relative to the DMSO control.  $n = 4$  independent experiments.  $**p = 0.0034$   $*p = 0.0267$  and  $p = 0.0411$ , for 1 h, 3 h and 6 h etoposide treatment, respectively; two-sided One Sample  $t$ -test. **o** Drug sensitivity to 72 h treatment with etoposide, between pseudo-diploid and highly-aneuploid clones treated with a sub-lethal dose (200 nM) of TAK632, or DMSO control.  $n = 5$  independent experiments.  $*p = 0.0258$  for SS48 versus SS51-SS111, two-sided unpaired  $t$ -test. **p** Viability following 72 h treatment with a sub-lethal dose (200 nM) of TAK632 or DMSO, in combination with PARP inhibition using olaparib (9  $\mu$ M) in pseudo-diploid vs. highly-aneuploid clones.  $n = 6$  independent experiments. Fold change calculated relative to the DMSO-treatment.  $*p = 0.0219$  for SS48 versus SS51-SS111; two-sided unpaired  $t$ -test. Source data are provided as a Source Data file.

immunotherapy<sup>70</sup>. In both datasets, we found that resistance to treatment was associated with high levels of the RAF/MEK/ERK pathway activity, specifically in highly-aneuploid tumors (Fig. 5q–r and Supplementary Fig. 9u, v).

Therefore, we propose that aneuploid cells increase CRAF/MEK/ERK pathway activity, which helps them overcome the elevated DNA damage. Inhibition of MEK/ERK signaling could therefore sensitize aneuploid cells to DNA damage inducers.

### RAF/MEK/ERK pathway activation is associated with chromosome gains independent of p53 status

Our isogenic RPE1 clones are *TP53*-WT, but highly-aneuploid cancer cells are mostly deficient for p53 activity<sup>6,7</sup>. We therefore knocked-down *TP53* using shRNAs, or knocked-out *TP53* using CRISPR/Cas9, to generate *TP53*-KD and *TP53*-KO RPE1 cells, respectively (Supplementary Fig. 10a–b). We validated the downregulation of p53 transcriptional targets in these p53-deficient cells (Supplementary Fig. 10c–i) and then assessed the activity of RAF/MEK/ERK pathway upon aneuploidy induction through reversine treatment. Reversine-induced aneuploidization in *TP53*-KD and *TP53*-KO cells resulted in a significant increase in the activity of CRAF (Supplementary Fig. 10j–m), MEK (Supplementary Fig. 10n–q) and ERK (Supplementary Fig. 10r–u), demonstrating that this pathway activation in this context is p53-independent.

To investigate whether our findings with trisomic cells also apply to monosomic cells, we turned to *TP53*-null RPE1 clones<sup>71</sup>. As expected, *TP53*-null cells experienced more DNA damage. However, monosomies did not further increase DNA damage in the cells (Supplementary Fig. 11a, b). Moreover, monosomic clones did not increase their RAF/MEK/ERK pathway activity, and in some of the monosomic clones the activity of this pathway was even reduced (Supplementary Fig. 11c–h). Accordingly, the monosomic clones did not show increased sensitivity to CRAF depletion in comparison to controls (Supplementary Fig. 11i, j). These results indicate that reliance on CRAF and the RAF/MEK/ERK pathway to overcome DNA damage is particularly characteristic of aneuploid cells with chromosome gains, revealing an important difference between these two classes of aneuploid cells.

## Discussion

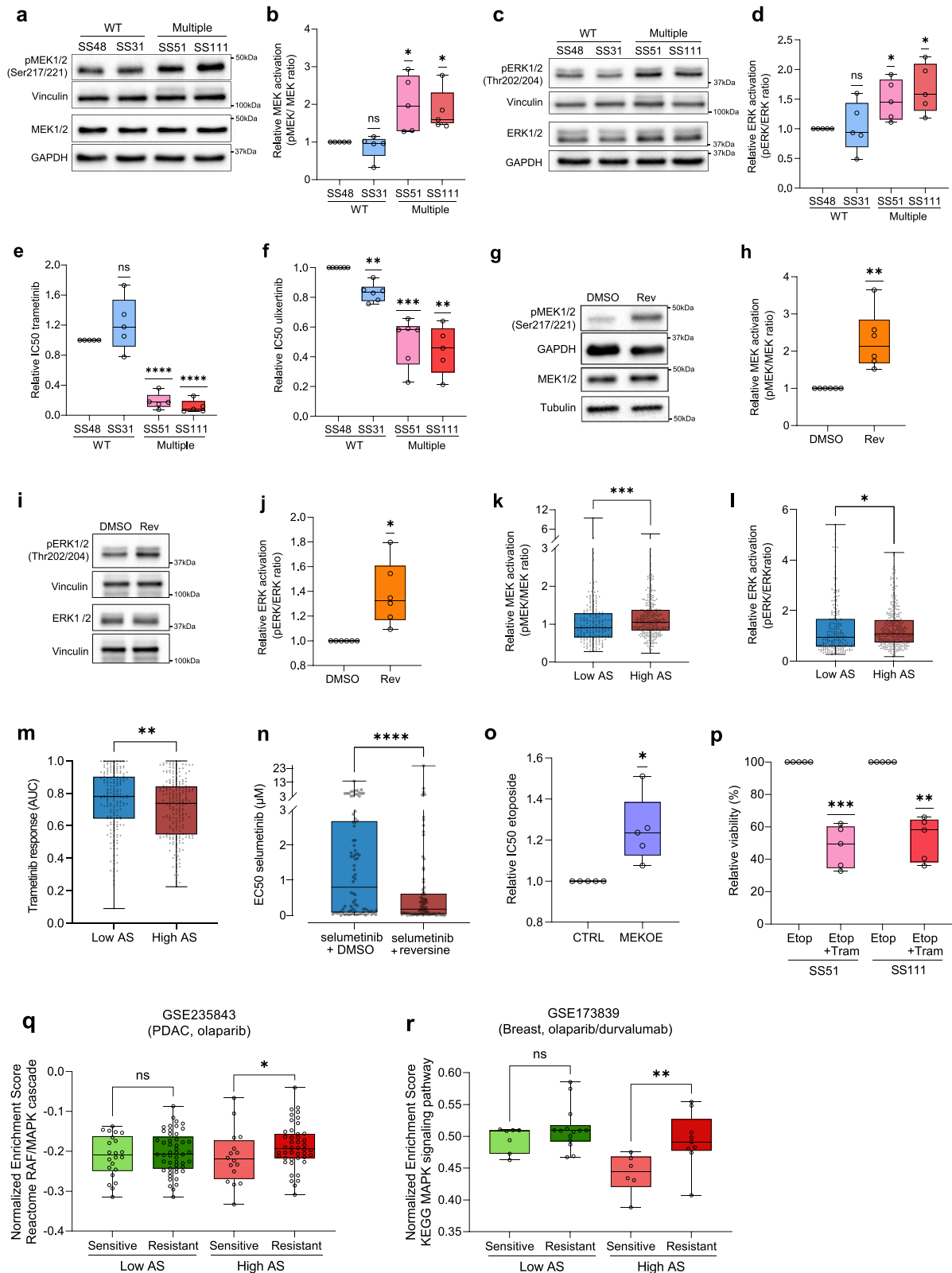
Aneuploidy has been recognized as a pervasive feature of tumors for over 100 years<sup>72</sup>. Recent sequencing technologies have confirmed that virtually all tumors harbor karyotypic abnormalities<sup>6</sup>. Nevertheless, research on aneuploidy has been hampered by the paucity of suitable

in vitro models and by the inability to disentangle aneuploidy from other co-existing features, such as p53 inactivation and genomic instability. Thus, understanding how karyotypic abnormalities affect cell physiology while controlling for potential confounders remains of paramount importance. Likewise, deconstructing the pathways deregulated by the aneuploid state holds the promise of unraveling unique dependencies exploitable for cancer therapy<sup>7</sup>.

To investigate the cellular and molecular consequences of aneuploidy, we have generated, characterized and analyzed a library of untransformed human cell lines with stable and defined aneuploid karyotypes. We employed multiple genomic, transcriptomic and functional assays to extensively profile this isogenic cell line library (Figs. 1, 2), and have incorporated these data sets into the Dependency Map ([www.depmap.org](http://www.depmap.org)), the PRIDE repository (<https://www.ebi.ac.uk/pride/>), and the Drug Repurposing Hub ([www.broadinstitute.org/drug-repurposing-hub](http://www.broadinstitute.org/drug-repurposing-hub)), in order to enable their broad use. Our own functional analyses and validation experiments revealed that aneuploid cells have increased activation of DDR and RNA metabolism, resulting in altered dependencies of aneuploid cells on these pathways.

### Increased dependency on RAF/MEK/ERK pathway activity

Aneuploidy has been previously reported to correlate with increased levels of DNA damage, mutational loads<sup>19,20</sup> and replication stress<sup>15–17,20–22,29,73</sup>. Here, by using our system of matched near-diploid and aneuploid cells, complemented by additional aneuploid systems and comprehensive analyses of human cancer cell lines, we found that cells with chromosome gains are more resistant to DNA damage inducers and to DDR perturbation in general (Fig. 3), in line with previous reports<sup>7,24,26,74,75</sup>. Our findings uncover the pathways triggered in response to DNA damage, and highlight the importance of RAF/MEK/ERK pathway activity, and of CRAF in particular (Fig. 4). CRAF has been implicated in DNA damage response through both kinase-dependent and kinase-independent mechanisms. CRAF kinase activity can directly feed into the RAF/MEK/ERK pathway to ensure proper execution of DDR<sup>56,57,76</sup>. RAF/MEK/ERK inhibitors have been reported to increase dependency on functional DDR<sup>67,68,77–79</sup>. In agreement with this, our data point at activation of RAF/MEK/ERK signaling in aneuploid cells, enabling them to tolerate DNA damage and keep proliferating in its presence (Fig. 5). These findings raise the exciting possibility to combine clinically-approved RAF/MEK/ERK inhibitors with DNA damage-inducing chemotherapies or PARP inhibitors for targeting aneuploid tumors.



RAF/MEK/ERK pathway activation in aneuploid cells has broader implications beyond the DDR. Activation of the RAF/MEK/ERK pathway occurs in ~40% of tumors<sup>80</sup> due to oncogenic mutations in this signaling cascade. Mutations in RAS and RAF genes—and of CRAF in particular—are linked to high degree of CIN and aneuploidy<sup>54,81–84</sup>, highlighting the importance of this pathway for the cellular response to aneuploidy. Notably, RPE1 cells are KRAS-mutant, but our findings

clearly indicate that the pathway does not reach its maximum activity in the parental population and is further activated following aneuploidy induction. Therefore, our data suggest that aneuploid tumors may benefit from treatment with RAF/MEK/ERK inhibitors regardless of genetic mutations in this pathway.

Several kinase-independent roles of CRAF have been reported as well, mainly relying on its scaffolding functions<sup>60,65,85–89</sup>. For example,

**Fig. 5 | Increased MEK/ERK pathway activity and dependency in aneuploid cells.** **a** Western Blot of pMEK1/2 (Ser217/221) and MEK1/2 in pseudo-diploid and highly-aneuploid clones. **b** Quantification of MEK1/2 activation (pMEK/MEK ratio).  $n = 5$  independent experiments;  $*p = 0.0383$  (SS51),  $p = 0.0247$  (SS11); two-sided One Sample  $t$ -test. **c** Western Blot of pERK1/2 (Thr202/Tyr204) and ERK1/2 in pseudo-diploid and highly-aneuploid clones. **d** Quantification of ERK1/2 activation (pERK/ERK ratio).  $n = 5$  independent experiments;  $*p = 0.0346$  (SS51) and  $p = 0.0223$  (SS11); two-sided One Sample  $t$ -test. **e** Sensitivity to 72 h drug treatment with the MEK inhibitor trametinib, in pseudo-diploid clones vs. highly-aneuploid clones. Fold-change calculated relative to SS48.  $n = 5$  independent experiments;  $****p = 6.6 \times 10^{-5}$  and  $p = 1.9 \times 10^{-5}$  for SS51 and SS11 respectively; two-sided one-sample  $t$ -test. **f** Sensitivity to 72 h drug treatment with the ERK inhibitor ulixertinib, in pseudo-diploid vs. highly-aneuploid clones. Fold-change calculated relative to SS48.  $n = 5$  independent experiments;  $**p = 0.0011$  (SS31) and  $p = 0.0016$  (SS11),  $***p = 0.0007$  (SS51); two-sided one-sample  $t$ -test. **g** Western blot of pMEK1/2 and total MEK1/2 in reversine-pulsed RPE1 cells. **h** Quantification of MEK activation in the reversine-pulsed cells, relative to the DMSO control.  $n = 6$  independent experiments.  $**p = 0.0096$ ; two-sided one-sample  $t$ -test. **i** Western blot of pERK1/2 and total ERK1/2 in reversine-pulsed RPE1 cells. **j** Quantification of ERK activation in reversine-treated cells, relative to the DMSO control.  $n = 6$  independent experiments.  $*p = 0.0148$ ; two-sided one-sample  $t$ -test. **k, l** Comparison of MEK (**k**) and

ERK (**l**) activity between the top and bottom aneuploidy quartiles of human cancer cell lines ( $n = 460$ ). Data obtained from DepMap 22Q1 release.  $***p = 0.0006$  (MEK);  $*p = 0.0424$  (ERK); two-tailed Mann–Whitney test. **m** Sensitivity to the MEK inhibitor trametinib in the top and bottom aneuploidy quartiles of human cancer cell lines ( $n = 412$ ). Data obtained from GDSC1 drug screen 22Q1 release.  $**p = 0.0069$ ; two-tailed Mann–Whitney test. **n** PRISM-based comparison of drug sensitivity to 120 h treatment with the MEK inhibitor selumetinib, between cancer cells treated with reversine (250 nM) or with control DMSO ( $n = 84$ ).  $****p = 5.3 \times 10^{-9}$ ; two-tailed Wilcoxon rank sum test. **o** Drug sensitivity to 72 h etoposide treatment, in RPE1 and MEK-overexpressing (MEK OE) RPE1 cells. Fold-change calculated relative to RPE1, per experiment.  $n = 5$  independent experiments;  $*p = 0.0256$ ; two-sided one-sample  $t$ -test. **p** Viability following 72 h treatment with a sub-lethal dose (0.45 nM) of the MEK inhibitor trametinib or DMSO, in combination with etoposide (2.5  $\mu$ M) in highly-aneuploid clones.  $n = 5$  independent experiments. Fold change calculated relative to etoposide-treated cells, per experiment;  $***p = 0.0009$  (SS51) and  $**p = 0.0015$  (SS11); two-sided one-sample  $t$ -test. **q** Comparison of the RAF/MEK/ERK pathway activity by ssGSEA in pancreatic PDxS (GSE235843) treated with olaparib.  $*p = 0.036$ ; one-tailed Mann–Whitney test. **r** Comparison of the RAF/MEK/ERK pathway activity by ssGSEA in breast tumors (GSE173839) treated with olaparib in combination with durvalumab.  $**p = 0.006$ ; one-tailed Mann–Whitney test. Source data are provided as a Source Data file.

CRAF has been shown to be pivotal in supporting the activation of CHK2, a crucial player in DDR<sup>65</sup>. Thus, the aneuploidy-induced CRAF dependency might also stem from CRAF's kinase-independent functions related to CHK2 activation. Intriguingly, however, aneuploid clones were less sensitive to *CHEK2* knockout yet more dependent on CRAF activity, suggesting that CHK2 activity might be largely dispensable in aneuploid cells. CRAF also plays a role in regulating Aurora B, PLK1 and Aurora A<sup>90,91</sup>, crucial mitotic players involved in chromosome segregation. Therefore, CRAF perturbation may result in DNA damage accumulated during aberrant mitoses. Nonetheless, the catalytic activity of CRAF seems to be more important than its non-catalytic one, otherwise: (1) RAF inhibitors, which cannot block the allosteric function of CRAF, would not work on aneuploid cells; and (2) MEK/ERK inhibition would not work on aneuploid cells, and MEK overexpression would not rescue the CRAF vulnerability. Future studies will be aimed at fully dissecting CRAF mode of action in response to DNA damage in aneuploid cells.

### RAF/MEK/ERK pathway activity and p53 activation

The p53 pathway is a major barrier for aneuploidy tolerance<sup>2,6,14,29</sup>. Aneuploidy-associated stresses, such as oxidative, metabolic, genotoxic and proteotoxic stresses, can lead to p53 activation followed by cell cycle arrest<sup>11,16,17,21,28,29,92</sup>. Aneuploidy-associated DNA damage can instigate p53 activation in several ways, including: lagging chromosomes broken by the cleavage furrow during chromosome mis-segregation<sup>14</sup>, ruptured micronuclei exposing their DNA to cytoplasmic nucleases<sup>93,94</sup>, segmental chromosomes generated by aneuploidy-induced genome instability and DNA replication stress<sup>16,17,21,29</sup>. Accordingly, our aneuploid clones show increased signs of DNA damage, high levels of p53 expression and upregulation of its target genes compared to pseudo-diploid counterparts (Fig. 3).

Notably, although p53 activation and aneuploidy-induced stresses are intimately intertwined, we found increased dependency on the RAF/MEK/ERK pathway independently of p53 status (Figs. 4, 5). Indeed, although we discovered these dependencies in *TP53*-WT cells, these effects remained significant when: (a) the aneuploid cells were compared to a near-diploid control clone harboring a p53-inactivating mutation (SS77) (Supplementary Figs. 2–3); (b) aneuploidy was induced in p53 knock-down or knock-out cells (Supplementary Fig. 10); and (c) hundreds of human cancer cell lines—most of them p53-inactivated—were stratified based on their aneuploidy scores, showing a positive correlation between the degree of aneuploidy and

RAF/MEK/ERK activation (Figs. 4, 5). We conclude that the identified vulnerabilities are a consequence of the aneuploid state per se. We note that our functional studies focused on aneuploid cells with extra chromosomes (trisomies), which is characteristic of most human tumors<sup>6,7</sup>. The consequences of monosomy differ from those of trisomy<sup>9</sup>, and chromosome losses did not significantly increase DNA damage and RAF/MEK/ERK activation, and did not increase the sensitivity of the cells to this pathway inhibition. Gains and losses should therefore be considered separately in functional dependency analyses of aneuploid cells.

### Limitations of the clone library

When generating the RPE1 clone library, DMSO-treated cells showed over 90% cloning efficiency, compared to just 4% for aneuploid clones. This reflects what is observed in human cancer, where most aneuploidies are selected against, with only certain ones recurring in a cancer type-specific manner<sup>6</sup>. Similarly, in human development, aneuploidy is the leading cause of miscarriages, with only a few trisomies (trisomies 13, 18 and 21) compatible with life<sup>95</sup>. However, the aneuploidies compatible with cell survival and proliferation are also those of most interest, and understanding how cells adapt to these aneuploidies could have clinical ramifications.

While the stable karyotype of our library is a technical advantage, the effects of aneuploidy may depend on the adaptation process. Studies in yeast show differences between the proteomes of naive and adapted aneuploid strains<sup>96</sup>. We confirmed that reduced sensitivity to DNA damage induction, alongside increased sensitivity to RAF/MEK/ERK inhibition, are general traits of aneuploid human cells, but other phenotypes might be specific to the method of aneuploidy induction and/or adaptation.

Our aneuploid clones were generated in RPE1 cells, which are widely used because they are untransformed and chromosomally stable. However, they lack a functional cGAS-STING pathway<sup>97</sup>, limiting their usage in contexts where this pathway is important, such as when studying the consequences of micronuclei<sup>98</sup>. Therefore, these cells are a good resource for studying aneuploidy, but the study of CIN, and of the combined effects of aneuploidy and CIN, would require a different model system, with a functional cGAS-STING pathway.

### Concluding remarks

Extensive DNA damage is one of the most prominent consequences of aneuploidy. Our work points at the central role of the RAF/MEK/ERK

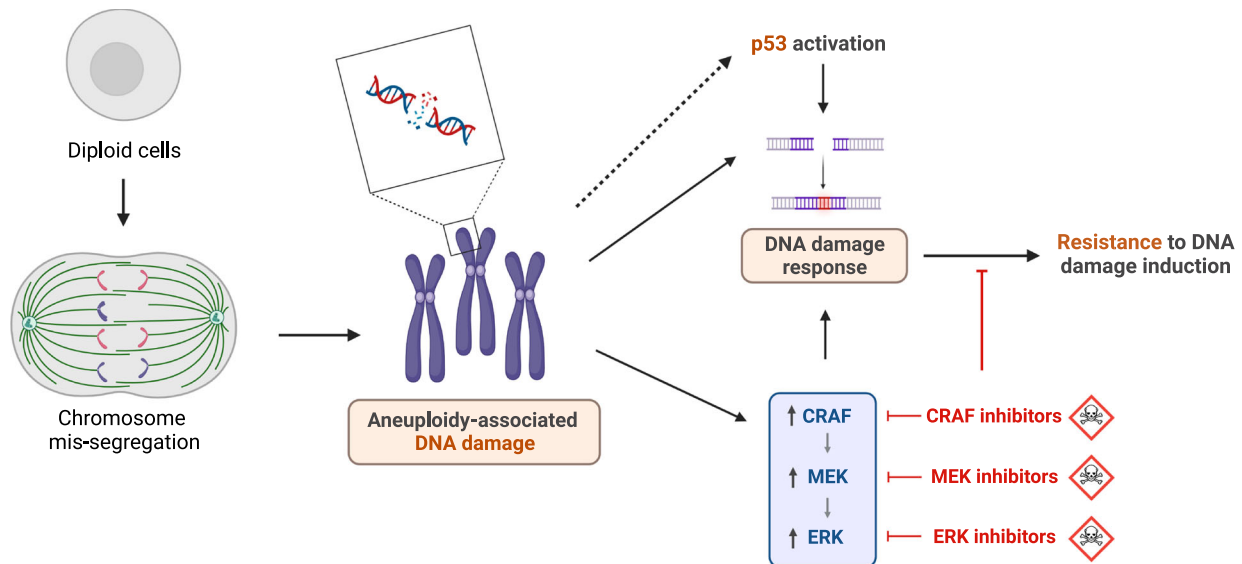


**Fig. 6 | Aneuploidy-induced DNA damage results in the upregulation of the CRAF/MEK/ERK pathway.** A summary illustration of the study. When cells become aneuploid following chromosome mis-segregation, they acquire DNA damage that activates the DNA damage response (DDR). When p53 is intact, this results in p53 pathway activation. The increased basal levels of DDR render the cells more resistant to further induction of DNA damage. In parallel, acquisition of DNA damage activates the CRAF/MEK/ERK pathway, which fuels the DNA damage response.

Consequently, aneuploid cells are more dependent than their diploid counterparts on CRAF, MEK, and ERK activity. Pharmacological induction of DNA damage further increases both the DNA damage response and the activation of CRAF/MEK/ERK pathway, and pharmacological inhibition of the CRAF/MEK/ERK pathway can thus sensitize aneuploid cells to DNA damage-inducing chemotherapies. The figure was created with BioRender.com.

pathway in overcoming DNA damage, enabling cells to tolerate this major aneuploidy-induced stress (Fig. 6). Our findings may have important implications for the selective targeting of aneuploid cancer cells by perturbing these pathways: selective inhibition of the RAF/MEK/ERK pathway, and of CRAF in particular, might sensitize aneuploid cancer cells to treatments with DNA damage inducers and PARP inhibitors. If these unique cellular vulnerabilities of chromosome gains hold true in the clinical setting, we speculate that they could be exploited for the selective eradication of aneuploid tumors.

## Methods

### Ethics

We attest that the research complies with all relevant ethical regulations.

### Cell culture

RPE1-hTERT cells (ATCC, RRID: CVCL\_4388), and all of their derivatives clones, CAL51 (DSMZ, RRID: CVCL\_1110) and SW48 (ATCC, RRID: CVCL\_1724) were cultured in DMEM (Life Technologies) with 10% fetal bovine serum (Sigma-Aldrich), 1% sodium pyruvate, 4 mM glutamine, 100 U/ml penicillin and 100 µg/ml streptomycin. BJ-hTERT cells (RRID: CVCL\_6573) were cultured in DMEM (Life Technologies) supplemented with 10% fetal bovine serum (Sigma-Aldrich), 4 mM glutamine, and 0.01 mg/mL hygromycin B. IMR90 cells (ATCC, RRID: CVCL\_C436) were cultured in EMEM supplemented with 2 mM glutamine, 1 mM sodium pyruvate and 0.1 mM non-essential amino-acids (ATCC), 10% fetal bovine serum, 100 U/mL penicillin and 100 U/ml penicillin and 100 µg/ml streptomycin. C1, C2, WA1, WA2, WA3 clones were cultured in 1:1 DMEM and F12 (Life Technologies) supplemented with 10% FBS, glutamax, 100U/ml penicillin and 100 µg/ml streptomycin. Cells were cultured at 37 °C with 5% CO<sub>2</sub> and are maintained in culture for a maximum of 3 weeks. All cell lines were tested free of mycoplasma contamination using Myco Alert (Lonza, Walkersville, MD, USA) according to the manufacturer's protocol.

To induce random aneuploidy, RPE1 cells were seeded and synchronized with 5 mM Thymidine for 24 h, then treated with 500 nM

reversine (or vehicle control) for 16 h. Read-outs were performed 72 h post reversine wash-out. CAL51, SW48, BJ-hTERT and IMR90 required 125 nM or 200 nM reversine for 24 h for CAL51 and SW48 respectively, and 500 nM reversine for 36hrs for both BJ-hTERT and IMR90.

Alternatively, cells were treated with 100 ng/mL nocodazole or 5 µM STLC for 14hrs, as previously described<sup>23</sup>. Briefly, arrested cells were collected and nocodazole or STLC were gently washed-out with PBS washes. Collected cells were reseeded and harvested 72 h post wash-out.

### Generation of a library of aneuploid clones

RPE1-hTERT cells were seeded in 10 cm dishes and treated with 500 nM reversine (or vehicle control) for 24 h. After drug (or vehicle control) wash-out, cells were kept in culture for 2 weeks and split regularly to keep them at about 70/80% confluence. Cells were then trypsinized and single-cell sorted in ~5000 well of multi-well plates containing conditioned medium (half of the final volume of the well). Single clones were then monitored over a month. Those able to proliferate over this period were transferred into 96 well plates and further expanded to 48, 24, 12 and 6 well plates. Clones were then transferred into 10 cm dishes and further propagated.

### Cell proliferation assay

RPE1-hTERT derived clones were plated in a 24-well plate support in at least three technical replicates. Cells were pictured every 4 h until reaching confluence using the Incucyte (Satorius). To estimate the confluency, the Built-In program (2021 A version) was used applying a threshold of 1 and a minimum area of 140 µm<sup>2</sup> to exclude the debris. Based on these proliferative curves, doubling time was calculated.

### Video microscopy

Live cell imaging was performed using an inverted microscope (Nikon Eclipse Ti) with a 20 x objective. The microscope was equipped with an incubation chamber maintained at 37 °C with 5% CO<sub>2</sub>. For experiments shown in Fig. 1 and Supplementary Figs. 1 and 4, RPE1-hTERT derived clones expressing a GFP-tagged version of H2b were seeded on 12-well

plates. Cells were filmed for 72 h every 5 min. For the positive control, cells were immediately treated with DMSO or reversine 500 nM. 80 cells for mitotic timing and 60 cells for chromosome segregation fidelity, both from four biological replicates, were analyzed using Fiji software.

### Whole exome sequencing and data analysis

WES data were generated as previously described<sup>62</sup>. Briefly, DNA library was constructed and sequenced using Illumina GAII-X. Paired-end DNA sequence reads were aligned to the human reference genome hg38. Raw WES data are available on the SRA database under the accession number PRJNA1144469. Mutation calling was performed as previously described<sup>62</sup>. Briefly, mutation analysis was performed using MuTect 1.1.6, default parameter in single sample mode. Heterozygous TP53 mutation was visualized using the Integrative Genomics Viewer (<https://software.broadinstitute.org/software/igv/>). Copy number calling was performed as previously described<sup>62</sup> using ABSOLUTE algorithm. Processed mutation and copy number calls are available in Supplementary Data 2–3 and on DepMap 21Q3 release ([https://figshare.com/articles/dataset/DepMap\\_21Q3\\_Public/15160110](https://figshare.com/articles/dataset/DepMap_21Q3_Public/15160110)). CNAs were defined as copy number values that deviated away from the chromosome-mean CNA value by  $>0.1$  ( $\log_2\text{CN}$ ) and  $>5$  SD (to remove noise, SD calculation excluded deviations  $>0.24$  away from the basal ploidy).

### RNAseq and data analysis

RNA was extracted in triplicates from each of the clones and the quality was assessed using Bioanalyzer 2100. For each sample, RNA library was prepared using TruSeq Stranded total RNA kit (Illumina) following manufacturer's protocol, and sequenced using TruSeq RNA UD Indices adapters (Illumina) on Novaseq 6000 sequencer (Illumina) following manufacturer's protocol. RNA sequence reads were aligned to the human reference genome hg38 using Bowtie2. Raw RNA reads are available on the SRA database under the accession number PRJNA889550. Normalized read counts, PCA analysis, and differential gene expression analysis were generated using DESeq2 R package<sup>99</sup>. Genes with  $<10$  normalized read counts were excluded from further analyses. A pre-ranked GSEA was performed on the differentially expressed genes using GSEA software 4.0.3, with the following parameters: 1000 permutations and Collapse analysis, using the Hallmark, KEGG, Biocarta, and Reactome gene sets (in separate analyses). For the pre-ranked GSEA analysis, genes with  $<20$  normalized read counts were excluded.

### miRNA profiling and data analysis

Total RNA, including small species, was isolated with the miRNeasy Mini Kit (Qiagen). Small RNA sequencing (sRNA-seq) libraries were prepared using 1000 ng of total RNA with the TruSeq Small RNA Kit (Illumina), following the manufacturer's protocol. Sequencing was performed on an Illumina Novaseq 6000 (50 bp single-read mode at a 12 million read depth per sample). Sequencing quality was checked in the FASTQC report, and only experiments with Q30 or above were considered (Phred Quality Score). Raw data together with detailed description of the procedures are available in the GEO database under accession number GSE247267. miRNA counting was performed with the *Isomirage* tool<sup>100</sup>: after counting, miRNA reads were normalized based on the library size (reads-per-million, using the sum of all miRNA-matching reads). Output table is available in Supplementary Data 6. Gene set enrichment analysis (GSEA) was performed on the final output table, comparing each RPE1 clone to reference pseudo-diploid RPE1-SS48 clone.

### Proteomics: data acquisition and data analysis

For sample preparation, 1000 cells per well in 96-well plates were lysed, reduced and alkylated using 40  $\mu\text{l}$  of 100 mM ammonium

bicarbonate (ABC), 40 mM CAA, and 10 mM TCEP buffer. The plate was sealed and incubated for 5 min at 95 °C while shaking. After bringing the samples to room temperature, droplets were removed by centrifugation and 200 ng of trypsin/LysC (Promega V5072) were added for protein digestion at 37 °C for 17 h (Benchmark Scientific IncuMix MP4). The reaction was stopped by addition of 10  $\mu\text{l}$  (10% v/v) formic acid.

Tryptic-digested cells were loaded on Evotip Pure tips following the manufacturer's protocol. Liquid chromatography-Mass Spectrometry (LC-MS) followed by data independent acquisition (DIA) was performed on an Evosep One system coupled to a Bruker timsTOF Pro 2 mass spectrometer, running DIA-PASEF. LC was carried out using the Evosep 30 SPD LC method (44 min gradient) with an EV1137 performance column (15 cm $\times$ 150  $\mu\text{m}$ , 1.5  $\mu\text{m}$ ) at 50 °C, coupled to 10  $\mu\text{m}$  ZDV (ZeroDeadVolume) captive Spray Emitter. For MS-acquisition, the Bruker default method "dia-PASEF-long gradient" was used. The acquisition scheme covered the mass range  $m/z$  400–1,201 and ion mobility range  $1/\text{KO}$  0.6–1.6, using 16 frames, with two precursor isolation windows per frame ( $m/z$  26 window width,  $m/z$  1.0 overlap between the adjacent windows). Accumulation and ramp times were set to 100 ms.

Raw data were processed using DIA-NN 1.8.1<sup>101</sup> (<https://github.com/vdemichiev/DiaNN>) with scan window size set to 7 and MS2 and MS1 mass accuracies set to 15 ppm. A spectral library free approach with the human reference proteome from UniProt<sup>102</sup> was used for peptide and protein annotation (UP00000564, downloaded 20230327) using the following settings: fragment  $m/z$  200–1800, N-terminal methionine excision enabled, maximum number of missed cleavages of 1, peptide length 7–50 amino acids, precursor  $m/z$  30–0–1800, precursor charge 1–4. The in-silico protease cleavage was at K and R, and cysteine carbamidomethylation was enabled as a fixed modification. The output was filtered at 1% FDR on peptide level, and is available in Supplementary Data 7. Raw data are available on the PRIDE database under accession number PXD048833. Gene set enrichment analysis (GSEA) was performed on the output table, comparing pseudo-diploid (RPE1-SS48 and RPE1-SS31) and highly-aneuploid (RPE1-SS51 and RPE1-SS111) clones.

### Genome-wide CRISPR screens and data analysis

Cells were barcoded and treated as previously described<sup>103</sup>. Briefly, aneuploid RPE1-hTERT clones were screened with the Avana library, which contains 73,372 guides with an average of 4 guides per gene, as previously described<sup>103</sup>. CRISPR dependency scores (CERES scores) were calculated as previously described<sup>103</sup> and were integrated with the data from all the cell lines screened as part of the Cancer Dependency Map, 21Q3 release ([https://figshare.com/articles/dataset/DepMap\\_21Q3\\_Public/15160110](https://figshare.com/articles/dataset/DepMap_21Q3_Public/15160110)). A pre-ranked GSEA was performed on the differentially-expressed genes using GSEA software 4.0.3, with the following parameters: 1000 permutations and Collapse analysis, using the Hallmark, KEGG, Biocarta, and Reactome gene sets (in separate analyses).

### Pharmacological screens and data analysis

Cells were screened against the Drug Repurposing Library from the Broad Institute<sup>41</sup>, as previously described<sup>47</sup>. Briefly, cells were seeded using a Multidrop™ Combi Reagent Dispenser (ThermoFisher) in a 384-well plate, 300 cells per well, in duplicate. 5336 compounds were tested at 2.5  $\mu\text{M}$ . All compounds were pre-plated onto the assay plates prior to cell addition using the Beckman Coulter Labcyte Echo. Seventy-two hours post-treatment, cell viability was assessed by Cell-TiterGlo® (Promega). The viability effect of each compound was calculated for each clone, and compared between the aneuploidy groups (RPE1-SS48 and RPE1-SS77 as near-diploid control clones, RPE1-SS6 and RPE1-SS119 as clones with single trisomies, RPE1-SS51 and RPE1-SS111 as clones with multiple trisomies). The percent activity of each

compound was determined by averaging the normalized activity of both replicates. The normalized activity was determined by the following equation—

$$N(x) = CR + \frac{x - \langle cr \rangle}{\langle sr \rangle - \langle cr \rangle} (SR - CR)$$

where  $N$  is the normalized activity value,  $x$  is the measured raw signal of a well,  $\langle cr \rangle$  is the median of the measured signal values of the Central Reference (DMSO control),  $\langle sr \rangle$  is the median of the measured signal values of the Scale Reference (Inhibitor control),  $CR$  is the desired median normalized value for the Central Reference (0), and  $SR$  is the desired median normalized value for the Scale Reference (−10 Genedata Screener and Spotfire were used in activity normalizations and hit calling). The activity threshold was set at the (negative) of three times the standard deviation of the DMSO control, the direction corresponding to activation or inhibition. Each compound was given one of three designations depending on their activity for each replicate. Compounds were classified as “Active” if the mean of both replicates was equal or less than the activity threshold. Compounds were classified as “Inconclusive” if one of the two replicates was equal or less than the activity threshold but the mean of both replicates was above the activity threshold. Compounds were classified as “Inactive” if neither of the replicates was equal or less than the activity threshold. Only drugs that led to a viability reduction ranging from −10% to −90% in all clones were considered. For comparisons of drugs targeting a specific pathway, a less stringent criterion was applied, so that only drugs that led to a viability reduction ranging from −10% to −90% in at least one category of cell lines were considered. All screening details are available in Supplementary Table 1.

### Drug treatments

Cells were seeded in a 96 w plate using Multidrop™ Combi Reagent Dispenser (ThermoFisher). Twenty-four hours later, cells were treated with drugs of interest. Alternatively, following aneuploidy induction, cells were washed with PBS to remove reversine and drugs were applied 4 h after seeding the cells. Cell viability was measured after 72 h of drug treatment using the MTT assay (Sigma M2128), with 500 µg/mL salt diluted in complete medium and incubated at 37 °C for 3 h. Formazan crystals were extracted using 10% Triton X-100 and 0.1 N HCl in isopropanol, and color absorption was quantified at 570 nm and 630 nm. Absolute IC50 for each drug was calculated using GraphPad PRISM 9.1, inhibitor vs. normalized response (four parameters) equation. All drugs details are available in Supplementary Table 2.

To test whether CRAF or MEK inhibition sensitized cells to DNA damage induction or to PARP inhibition, RPE1-SS48, RPE1-SS51 and RPE1-SS111 were seeded in triplicates in 96-well plates. Cells were treated with serial dilutions of etoposide or with 9 µM olaparib (=IC50 for this drug in RPE1-SS48 cells) in combination with 200 nM TAK632 (or vehicle control), or 0.45 nM trametinib (or vehicle control) in combination with 2.5 µM etoposide, for 72 h. Cell viability was measured using the MTT assay (Sigma M2128).

### Immunofluorescence

Cells were washed with PBS and then fixed for 15 min at room temperature (RT) with 4% para-formaldehyde, followed by permeabilization with Triton X-100 0.5% for 5 min at RT, and quenching reduction with L-Glycin 0.1 M in PBS for 15 min at RT. Slides were then blocked for 30 min at RT in blocking solution containing 10% goat serum, 3% BSA, L-Glycin 1%, NaCl 150 mM, TRIS pH7.5 10 mM, and 0.1% Triton X-100. Slides were incubated with primary antibody against 53BP1 (1:1000, Abcam) or phospho-histone Ser139 γH2AX (1:1000, Millipore) in blocking solution for 1.5 h at RT in a humid chamber. After washing with PBS, cells were incubated with Alexa Fluor 488 or Alexa Fluor 555 tagged anti-mouse antibody (1:1000, Cell Signaling Technologies) for 1 h at

RT in a humid black chamber, and then stained with DAPI (1 µg/mL) diluted in PBS for 3 min at RT in a humid black chamber. Images were acquired using cellSens Imaging Software (Olympus), and merged using ImageJ. The number of foci per cell was counted using CellProfiler (BroadInstitute), using Otsu 3 parameters mathematical model for nuclei and foci definition, with foci size of at least 4px and 0.1 intensity.

Where specified, immunofluorescence was combined with EdU detection. Briefly, cells were treated with EdU for 8 h and fixed. After washing, cells were fixed and the slides were blocked for 30' with the blocking solution. EdU detection was performed using click-it EdU Cell Proliferation kit for Imaging (ThermoFisherScientific) according to the manufacturer's protocol. At the end of the procedure, cells were incubated with primary antibodies, followed by the subsequent steps of immunofluorescence procedures as previously described.

### Western blots

Cells were lysed in NP-40 lysis buffer (1% NP-40;150 mM NaCl; 50 mM Tris HCl pH 8.0) with the addition of protease inhibitor cocktail (Sigma-Aldrich #P8340) and phosphatase inhibitor cocktail (Sigma Aldrich #P0044). Protein lysates were sonicated (Biovector) for 5 min (30 s on/30 s off) at 4 °C, then centrifuged at maximum speed for 15 min and resolved on 12% SDS-PAGE gels. Bands were detected using chemiluminescence (Millipore #WBLUR0500) on Fusion FX gel-doc (Vilber). All antibodies details are available in Supplementary Table 2.

### qRT-PCR

Cells were harvested using Bio-TRI® (Bio-Lab) and RNA was extracted following manufacturer's protocol. cDNA was amplified using GoScript™ Reverse Transcription System (Promega) following the manufacturer's protocol. qRT-PCR was performed using Sybr® green, and quantification was performed using the ΔCT method. All primer sequences are available in Supplementary Table 2.

### Dependency map data analysis

Aneuploidy scores (AS) of each cell line were assigned following similar principles to those used by Cohen-Sharir et al.<sup>7</sup>. Briefly, the median relative copy number was calculated per chromosome arm, the variation across chromosome arms was evaluated, and the number of chromosome arms that deviate from the basal ploidy was determined as the aneuploidy score. Code is available at [https://github.com/BenDavidLab/Ploidy\\_And\\_AS\\_Zerbib-et-al\\_2024](https://github.com/BenDavidLab/Ploidy_And_AS_Zerbib-et-al_2024). The resultant aneuploidy score list is available in Supplementary Data 10. mRNA gene expression values, protein expression values, CRISPR and RNAi dependency scores (Chronos and DEMETER2 scores, respectively) were obtained from DepMap 22Q1 release ([https://figshare.com/articles/dataset/DepMap\\_22Q1\\_Public/19139906](https://figshare.com/articles/dataset/DepMap_22Q1_Public/19139906)), and compared between the bottom (AS ≤ 8) and top (AS ≥ 21) aneuploidy quartiles.

For doubling time analyses, the doubling time (DT) of each cell line was assigned as previously published<sup>45</sup>. mRNA expression values were floored to  $\log_2(\text{TPM} + 1) = 0.1$ . Within the bottom quartile (AS ≤ 8) and the top quartile (AS ≥ 21), DT was correlated to gene expression utilizing a linear model (lm function in R studio v4.1.1, with lineage as a covariate, using the equation: gene-DT+lineage), following the method of Taylor et al. Genes were determined as overexpressed in highly proliferative aneuploid cancer cells if they were significantly associated with DT within the top AS quartile but not within the bottom AS quartile. Significance thresholds:  $(\log_{10}(p\text{-value}) \geq 2.5)$  OR  $(-\log_{10}(p\text{-value}) \geq 1.3)$  AND correlation coefficient  $< -0.005$ . The resultant list of genes is available in Supplementary Data 11. This list was subjected to gene set enrichment analysis using the ‘Hallmark’, ‘KEGG’, ‘Reactome’ and ‘Gene Ontology Biological Processes’ gene set collections from MSigDB (<http://www.gsea-msigdb.org/gsea/msigdb/>)<sup>39,104</sup>.

For doubling time-controlled PRISM screen analysis, PRISM sensitivity results were obtained from DepMap 23Q2 release, and limma R package with doubling time as covariate was run, comparing the

bottom quartile ( $AS \leq 8$ ) and the top quartile ( $AS \geq 21$ ) of aneuploidy scores, as previously described<sup>7</sup>.

Analysis of CRAF, MEK and ERK protein activity was performed by measuring the ratio between the phosphor-protein to the total protein levels, based on an RPPA protein array<sup>62</sup>. Quantification of total proteins was based on the DepMap proteomics data<sup>63</sup>. For correlation between RAF pathway activity and drug response, Spearman correlation was performed between pCRAF/CRAF, pMEK/MEK and pERK/ERK protein ratio from the RPPA protein array datasets and the drug response of each tested drug in the CTD<sup>2</sup> drug screen. Only significant spearman correlation values were compared between DNA-damage inducing (DDR) drugs and other drugs—no drugs passed the significance threshold when comparing MEK activity and response to drugs, therefore only correlations between CRAF and ERK activity and drug response were presented.

### TCGA data analysis

TCGA data were retrieved using TCGAbiolinks R package<sup>105</sup>. Aneuploidy scores (AS) were obtained from Taylor et al.<sup>6</sup>, and correlated to tumor gene expression using lineage as a covariate (lm function in R studio v4.1.1, using the equation:  $gene-AS+lineage$ ), as previously described<sup>6</sup>. Genes were ranked based on their aneuploidy score coefficient, and then subjected to pre-ranked gene set enrichment analysis<sup>39</sup> using the 'Hallmark', 'Biocarta', 'KEGG', and 'Reactome' gene set collections from MSigDB.

### siRNA experiments

RPE1-hTERT cells were transfected with siRNAs against CRAF (ONTARGETplus SMART-POOL<sup>®</sup>, Dharmacon), or with a control siRNA (ONTARGETplus SMART-POOL<sup>®</sup>, Dharmacon) using Dharmafect1 (Dharmacon) following manufacturers' protocols. RPE1-hTERT cells were transfected with 1 nM of siRNAs against CRAF or against BRAF or with scrambled siRNAs (individual oligos, Sigma-Aldrich) using Lipofectamine RNAiMAX (Invitrogen) following manufacturer's protocol. To test whether aneuploidy induction sensitized cells to CRAF, RPE1-hTERT cells were seeded and synchronized with Thymidine 5 mM for 24 h then treated with reversine 500 nM for 20 h. Similarly, CAL51 and IMR90 were treated with 125 nM reversine for 24 h or 500 nM for 36 h, respectively. After the reversine pulse, cells were transfected with siRNA against CRAF (SMART-POOL<sup>®</sup> from Dharmacon or individual oligos from Sigma-Aldrich) using Lipofectamine<sup>®</sup> RNAiMAX (Invitrogen) following the manufacturer's protocol. Cell growth following siRNA transfection was followed by live cell imaging using Incucyte<sup>®</sup> (Satorius). The effect on proliferation or viability were calculated by comparing the fold-change of doubling time of the cells or cell number in the targeted siRNA vs. control siRNA wells at 72 h post-transfection. For visualization, the cell borders were highlighted using AI-trained Ilastik<sup>®</sup> software. Sequences of individual oligos are available in Supplementary Table 2.

### Live cell imaging using LiveCyte<sup>®</sup>

2000 cells were seeded in triplicates in microscopy-compatible 96-well plates (Corning), and were treated for 72 h with 10  $\mu$ M of 8-Br-cAMP. Cells were imaged every 20 min for 72 h using LiveCyte<sup>®</sup> (Phase Focus), with an inverted microscope at 10X objective (microscope placed in an incubation chamber maintained at 37 °C with 5% CO<sub>2</sub>). Images were acquired using the LiveCyte acquisition software, and single-cell tracking, segmentation and analyses was performed using the LiveCyte analysis software (Phase Focus). Cell doubling time, dry mass doubling time, cellular area and perimeter, instantaneous velocity and track speed were calculated by the automatic LiveCyte<sup>®</sup> analysis software (Phase Focus).

### Flow cytometry analysis

For cell cycle analysis, 70% confluent RPE1-hTERT clones were collected and fixed with ice-cold 70% ethanol for 2 h on ice. Ethanol was

then washed and cells were stained with 50  $\mu$ g/mL Propidium Iodine (BioLegend) and 0.1 mg/mL RNase A (Invitrogen) in PBS for 10 min RT. Flow cytometry acquisition was performed on CytoFLEX<sup>®</sup> (Beckman Coulter) and data analysis was performed using CytExpert v2.4 analysis software (Beckman Coulter). Gating of living cells and singlet was common in all the analyzed samples, gating of cell cycle phase was specific to each sample. Example of the gating strategy is available in Supplementary Fig. 12a.

For cell death analysis, 100,000 cells were seeded in a 6-well plate and treated for 72 h with 10  $\mu$ M of 8-Br-cAMP, and with Etoposide 2.5  $\mu$ M for 72 h as a positive control. Cells were stained with SYTOX<sup>™</sup> Green Ready Flow<sup>™</sup> Reagent (Invitrogen), following the manufacturer's protocol. Flow cytometry acquisition was performed using CytoFLEX<sup>®</sup> (Beckman Coulter) and data analysis was performed using Kaluza Analysis software 2.1 (Beckman Coulter). The gating of living cells and singlets was common in all the analyzed samples, per experiment. Gating of positive cells (defined as upper half of the pick in etoposide-treated cells) was defined per cell line. Example of the gating strategy is available in Supplementary Fig. 12b–d.

### Generation of genetically engineered RPE1 cells

Lentiviral preparation of *TP53* shRNA and MEK overexpression constructs were obtained by transfecting lentiviral packaging vectors (pMDL, pRev, VSVG), and inducible Tet-pLKO-neo (Addgene #21916) cloned with sh*TP53* or pHAGE-MAP2K1 plasmid (Addgene #116757) in HEK293T cells, using JETPei<sup>®</sup> (Polyplus) following the manufacturer's protocol. Lentiviral preparation was collected and RPE1-hTERT cells were transduced with 1 mg/mL polybrene (Sigma-Aldrich). Cells were selected 800  $\mu$ l/ml G418 (sh*TP53*) or using 1 mg/mL puromycin (MEK-OE) for a week. *TP53* knockdown and MEK overexpression were validated by western-blot over nutlin-3a stimulation or at steady state for *TP53*-KD and MEK-OE respectively. *TP53*-KO RPE1 cells were kindly provided by Jallepalli Lab<sup>28</sup>. Sequences, plasmids and antibodies references are available in Supplementary Table 2.

### PRISM screen

PRISM screen was performed as previously described<sup>7,47</sup>. Briefly, cells were plated in triplicate in 384-well plates at 1250 cells per well. Cells were treated with the MEK inhibitor selumetinib (8 concentrations of threefold dilutions, ranging from 0.9 nM to 20  $\mu$ M) in presence of reversine (250 nM) or DMSO for 5 days. Cells were then lysed, and lysate plates were pooled for amplification and barcode measurement. Viability values were calculated by taking the median fluorescence intensity of beads corresponding to each cell line barcode, and normalizing them by the median of DMSO control. Dose-response curves and EC50 values were calculated by fitting four-parameter curves to viability data for each cell line, using the R drc package<sup>106</sup>, fixing the upper asymptote of the logistic curves to 1. EC50 comparisons were performed on the 84 cell lines for which well-fit curves ( $r^2 > 0.3$ ) were generated.

### Clinical datasets analyses

Drug response data from pancreatic adenocarcinoma patient-derived xenografts (PDXs) (GSE235843) and from a clinical trial with breast cancer patients (GSE173839), were obtained and segregated according to their response to PARP inhibitor treatment, as described in their associated papers<sup>69,70</sup>. Gene set enrichment analysis (GSEA) was performed between resistant and sensitive tumors to PARP inhibitors using GSEapy python package<sup>107</sup>. RNA-based inference of gene level CNV was performed using CNVkit<sup>108</sup> and CAFE<sup>109</sup> algorithms, for RNAseq and microarray data, respectively. Aneuploidy scores were determined by counting the number of chromosome arms that deviate from the basal ploidy inferred from gene level CNV using ASCETS<sup>110</sup>. Single sample GSEA (ssGSEA) analysis was performed in both datasets to evaluate gene expression of selected gene sets in each tumor.



Tumors were segregated according to their aneuploidy score: top 25% vs bottom 25%, and top 50% vs bottom 50%, for GSE235843 and GSE173839, respectively. ssGSEA scores were compared between resistant and sensitive tumors to PARP inhibitors in each aneuploidy group.

Drug response data from the pediatric PDX cohort was obtained (EA00001002528) and tumors were separated based on their response to drugs of interest as described in the associated paper<sup>64</sup>. Copy number calling was performed using CONCERTING algorithm, and kindly provided by Dr. Jiyang Yu. PDX responses to RAF inhibitors and trametinib were compared according to their aneuploidy scores (top 25% vs bottom 25%).

### Statistics and reproducibility

The number of cells used for each experiment is available in the method section. Western Blot quantifications were performed using ImageJ<sup>®</sup>. The numbers of independent experiments and analyzed cell lines of each computational analysis are available in the figure legends. No statistical method was used to predetermine sample size, no data were excluded from the analyses, the experiments were not randomized, and the investigators were not blinded to allocation during experiments and outcome assessment. Statistical analyses were performed using GraphPad PRISM<sup>®</sup> 9.1. Details of each statistical test are indicated in the figure legends. In each presented box plot, whiskers are minimum and maximum values, the internal bar represents the median of the distribution, the box represents the 25th and 75th quartile. In Figs. 1e, 3c and Supplementary Figs. 1e, 4c, d, 5i, 11b, the bar represents the mean and SEM. Significance thresholds were defined as  $p$ -value = 0.05 and  $q$ -value = 0.25.

### Reporting summary

Further information on research design is available in the Nature Portfolio Reporting Summary linked to this article.

### Data availability

Aneuploid RPE1-hTERT clones generated in this study are available upon request to Stefano Santaguida. Low-pass whole-genome sequencing, Whole Exome Sequencing and RNA sequencing data are available in the SRA database under accession numbers PRJNA672256, PRJNA1144469 and PRJNA889550 respectively. Genome-wide CRISPR/Cas9 screening data of RPE1-hTERT clones are available in the DepMap database 2IQ3 release ([https://figshare.com/articles/dataset/DepMap\\_2IQ3\\_Public/15160110](https://figshare.com/articles/dataset/DepMap_2IQ3_Public/15160110)). miRNA expression data are available in the GEO database (<https://www.ncbi.nlm.nih.gov/geo/>) under the accession number GSE247267. Protein expression raw data are available in the PRIDE database under the accession number PXD048833. Drug screen data are available in the Drug Repurposing Hub (<https://repo-hub.broadinstitute.org/repurposing#home>). Cancer cell line expression, CRISPR/Cas9 and RNAi data are available in the DepMap database 22Q1 release ([https://figshare.com/articles/dataset/DepMap\\_22Q1\\_Public/19139906](https://figshare.com/articles/dataset/DepMap_22Q1_Public/19139906)). All data are publicly available as of the date of publication. All output tables are available within the article, as Supplementary Information, Supplementary Data, or Source Data files. All previously published clinical datasets are available as following: Pediatric PDXs (EGAS00001002528, <https://doi.org/10.1038/nature23647>), PDAC PDXs (GSE235843, <https://doi.org/10.1158/2159-8290.CD-22-0412>), Breast tumors (GSE173839, <https://doi.org/10.1016/j.ccell.2021.05.009>). Source data for all presented graphs and Western Blots are provided with this paper. Source data are provided with this paper.

### Code availability

Code extension to the aneuploidy score of cancer cell lines presented in Cohen-Sharir et al.<sup>7</sup> can be downloaded from [https://github.com/BenDavidLab/Ploidy\\_And\\_AS\\_Zerbib-et-al\\_2024](https://github.com/BenDavidLab/Ploidy_And_AS_Zerbib-et-al_2024). Aneuploidy scores are available as Supplementary Data 10.

## References

- Ben-David, U. & Amon, A. Context is everything: aneuploidy in cancer. *Nat. Rev. Genet.* **21**, 44–62 (2020).
- Santaguida, S. & Amon, A. Short- and long-term effects of chromosome mis-segregation and aneuploidy. *Nat. Rev. Mol. Cell Biol.* **16**, 473–485 (2015).
- Vasudevan, A. et al. Aneuploidy as a promoter and suppressor of malignant growth. *Nat. Rev. Cancer* **21**, 89–103 (2021).
- Zhu, J., Tsai, H. J., Gordon, M. R. & Li, R. Cellular stress associated with aneuploidy. *Dev. Cell* **44**, 420–431 (2018).
- Chunduri, N. K. & Storchová, Z. The diverse consequences of aneuploidy. *Nat. Cell Biol.* **21**, 54–62 (2019).
- Taylor, A. M. et al. Genomic and functional approaches to understanding cancer aneuploidy. *Cancer Cell* **33**, 676–689.e3 (2018).
- Cohen-Sharir, Y. et al. Aneuploidy renders cancer cells vulnerable to mitotic checkpoint inhibition. *Nature* **590**, 486–491 (2021).
- Kuznetsova, A. Y. et al. Chromosomal instability, tolerance of mitotic errors and multidrug resistance are promoted by tetraploidization in human cells. *Cell Cycle* **14**, 2810–2820 (2015).
- Chunduri, N. K. et al. Systems approaches identify the consequences of monosomy in somatic human cells. *Nat. Commun.* **12**, 1–17 (2021).
- Rutledge, S. D. et al. Selective advantage of trisomic human cells cultured in non-standard conditions. *Sci. Rep.* **6**, 1–12 (2016).
- Stingele, S. et al. Global analysis of genome, transcriptome and proteome reveals the response to aneuploidy in human cells. *Mol. Syst. Biol.* **8**, 608 (2012).
- Kneissig, M. et al. Micronuclei-based model system reveals functional consequences of chromothripsis in human cells. *Elife* **8**, e50292 (2019).
- Garribba, L. & Santaguida, S. The dynamic instability of the aneuploid genome. *Front. Cell Dev. Biol.* **10**, 838928 (2022).
- Janssen, A., Van Der Burg, M., Szuhai, K., Kops, G. J. P. L. & Medema, R. H. Chromosome segregation errors as a cause of DNA damage and structural chromosome aberrations. *Science* **333**, 1895–1898 (2011).
- Lamm, N. et al. Genomic instability in human pluripotent stem cells arises from replicative stress and chromosome condensation defects. *Cell Stem Cell* **18**, 253–261 (2016).
- Passerini, V. et al. The presence of extra chromosomes leads to genomic instability. *Nat. Commun.* **7**, 1–12 (2016).
- Santaguida, S., Richardson, A., Rhind, N., Desai, A. & Amon, A. Chromosome mis-segregation generates cell-cycle-arrested cells with complex karyotypes that are eliminated by the immune system. *Dev. Cell* **41**, 638–651 (2017).
- Umbreit, N. T. et al. Mechanisms generating cancer genome complexity from a single cell division error. *Science* **368**, eaba0712 (2020).
- Sheltzer, J. M. et al. Aneuploidy drives genomic instability in yeast. *Science* **333**, 1026–1030 (2011).
- Blank, H. M., Sheltzer, J. M., Meehl, C. M. & Amon, A. Mitotic entry in the presence of DNA damage is a widespread property of aneuploidy in yeast. *Mol. Biol. Cell* **26**, 1440–1451 (2015).
- Garribba, L. et al. Short-term molecular consequences of chromosome mis-segregation for genome stability. *Nat. Commun.* **14**, 1–17 (2023).
- Burrell, R. A., McGranahan, N., Bartek, J. & Swanton, C. The causes and consequences of genetic heterogeneity in cancer evolution. *Nature* **501**, 338–345 (2013).
- Ippolito, M. R. et al. Gene copy-number changes and chromosomal instability induced by aneuploidy confer resistance to chemotherapy. *Dev. Cell* **56**, 2440–2454.e6 (2021).
- Lee, A. J. X. et al. Chromosomal instability confers intrinsic multidrug resistance. *Cancer Res.* **71**, 1858–1870 (2011).

25. Lukow, D. A. et al. Chromosomal instability accelerates the evolution of resistance to anti-cancer therapies. *Dev. Cell* **56**, 2427–2439.e4 (2021).
26. Replogle, J. M. et al. Aneuploidy increases resistance to chemotherapeutics by antagonizing cell division. *Proc. Natl. Acad. Sci. USA* **117**, 30566–30576 (2020).
27. Santaguida, S., Tighe, A., D'Alise, A. M., Taylor, S. S. & Musacchio, A. Dissecting the role of MPS1 in chromosome biorientation and the spindle checkpoint through the small molecule inhibitor reversine. *J. Cell Biol.* **190**, 73–87 (2010).
28. Santaguida, S., Vasile, E., White, E. & Amon, A. Aneuploidy-induced cellular stresses limit autophagic degradation. *Genes Dev.* **29**, 2010–2021 (2015).
29. Soto, M. et al. p53 prohibits propagation of chromosome segregation errors that produce structural aneuploidies. *Cell Rep.* **19**, 2423–2431 (2017).
30. Bakker, B. et al. Single-cell sequencing reveals karyotype heterogeneity in murine and human malignancies. *Genome Biol.* **17**, 1–15 (2016).
31. Klaasen, S. J. et al. Nuclear chromosome locations dictate segregation error frequencies. *Nature* **607**, 604–609 (2022).
32. Williams, B. R. et al. Aneuploidy affects proliferation and spontaneous immortalization in mammalian cells. *Science* **322**, 703–709 (2008).
33. Torres, E. M. et al. Effects of aneuploidy on cellular physiology and cell division in haploid yeast. *Science* **317**, 916–924 (2007).
34. Tang, Y. C., Williams, B. R., Siegel, J. J. & Amon, A. Identification of aneuploidy-selective antiproliferation compounds. *Cell* **144**, 499–512 (2011).
35. He, L. et al. A microRNA component of the p53 tumour suppressor network. *Nature* **447**, 1130–1134 (2007).
36. Navarro, F. & Lieberman, J. miR-34 and p53: new insights into a complex functional relationship. *PLoS ONE* **10**, e0132767 (2015).
37. Hermeking, H. MicroRNAs in the p53 network: micromanagement of tumour suppression. *Nat. Rev. Cancer* **12**, 613–626 (2012).
38. Mootha, V. K. et al. PGC-1 $\alpha$ -responsive genes involved in oxidative phosphorylation are coordinately downregulated in human diabetes. *Nat. Genet.* **34**, 267–273 (2003).
39. Subramanian, A. et al. Gene set enrichment analysis: A knowledge-based approach for interpreting genome-wide expression profiles. *Proc. Natl. Acad. Sci. USA* **102**, 15545–15550 (2005).
40. Ippolito, M. R. et al. Increased RNA and protein degradation is required for counteracting transcriptional burden and proteotoxic stress in human aneuploid cells. *Cancer Discov.* <https://doi.org/10.1101/2023.01.27.525826> (2024).
41. Corsello, S. M. et al. The drug repurposing hub: a next-generation drug library and information resource. *Nat. Med.* **23**, 405–408 (2017).
42. Caldecott, K. W. Single-strand break repair and genetic disease. *Nat. Rev. Genet.* **9**, 619–631 (2008).
43. Scully, R., Panday, A., Elango, R. & Willis, N. A. DNA double-strand break repair-pathway choice in somatic mammalian cells. *Nat. Rev. Mol. Cell Biol.* **20**, 698–714 (2019).
44. den Hollander, A. I. et al. Mutations in a human homologue of *Drosophila* crumbs cause retinitis pigmentosa (RP12). *Nat. Genet.* **23**, 217–221 (1999).
45. Tsherniak, A. et al. Defining a cancer dependency map. *Cell* **170**, 564–576.e16 (2017).
46. Basu, A. et al. An interactive resource to identify cancer genetic and lineage dependencies targeted by small molecules. *Cell* **154**, 1151 (2013).
47. Corsello, S. M. et al. Discovering the anticancer potential of non-oncology drugs by systematic viability profiling. *Nat. Cancer* **1**, 235–248 (2020).
48. Garnett, M. J. et al. Systematic identification of genomic markers of drug sensitivity in cancer cells. *Nature* **483**, 570–575 (2012).
49. Yang, W. et al. Genomics of drug sensitivity in cancer (GDSC): a resource for therapeutic biomarker discovery in cancer cells. *Nucleic Acids Res.* **41**, D955–D961 (2013).
50. Okaniwa, M. et al. Discovery of a selective kinase inhibitor (TAK-632) targeting pan-RAF inhibition: design, synthesis, and biological evaluation of C-7-substituted 1,3-benzothiazole derivatives. *J. Med. Chem.* **56**, 6478–6494 (2013).
51. Dumaz, N., Light, Y. & Marais, R. Cyclic AMP blocks cell growth through Raf-1-dependent and Raf-1-independent mechanisms. *Mol. Cell Biol.* **22**, 3717–3728 (2002).
52. Cui, Y. & Guadagno, T. M. B-RafV600E signaling deregulates the mitotic spindle checkpoint through stabilizing Mps1 levels in melanoma cells. *Oncogene* **27**, 3122–3133 (2008).
53. Cui, Y., Borysova, M. K., Johnson, J. O. & Guadagno, T. M. Oncogenic B-RafV600E induces spindle abnormalities, supernumerary centrosomes, and aneuploidy in human melanocytic cells. *Cancer Res.* **70**, 675–684 (2010).
54. Kamata, T. et al. BRAF inactivation drives aneuploidy by deregulating CRAF. *Cancer Res.* **70**, 8475–8486 (2010).
55. Herman, J. A. et al. Hyper-active RAS/MAPK introduces cancer-specific mitotic vulnerabilities. *Proc. Natl. Acad. Sci. USA* **119**, e2208255119 (2022).
56. Garnett, M. J., Rana, S., Paterson, H., Barford, D. & Marais, R. Wild-type and mutant B-RAF activate C-RAF through distinct mechanisms involving heterodimerization. *Mol. Cell* **20**, 963–969 (2005).
57. Rushworth, L. K., Hindley, A. D., O'Neill, E. & Kolch, W. Regulation and role of Raf-1/B-Raf heterodimerization. *Mol. Cell Biol.* **26**, 2262–2272 (2006).
58. Karoulia, Z. et al. An integrated model of RAF inhibitor action predicts inhibitor activity against oncogenic BRAF signaling. *Cancer Cell* **30**, 485–498 (2016).
59. Zhang, C. et al. RAF inhibitors that evade paradoxical MAPK pathway activation. *Nature* **526**, 583–586 (2015).
60. Venkatanarayan, A. et al. CRAF dimerization with ARAF regulates KRAS-driven tumor growth. *Cell Rep.* **38**, 110351 (2022).
61. Wellbrock, C., Karasarides, M. & Marais, R. The RAF proteins take centre stage. *Nat. Rev. Mol. Cell Biol.* **5**, 875–885 (2004).
62. Ghandi, M. et al. Next-generation characterization of the cancer cell line encyclopedia. *Nature* **569**, 503–508 (2019).
63. Nusinow, D. P. et al. Quantitative proteomics of the cancer cell line encyclopedia. *Cell* **180**, 387–402.e16 (2020).
64. Stewart, E. et al. Orthotopic patient-derived xenografts of paediatric solid tumours. *Nature* **549**, 96–100 (2017).
65. Advani, S. J. et al. Kinase-independent role for CRAF-driving tumour radioresistance via CHK2. *Nat. Commun.* **6**, 1–8 (2015).
66. Golding, S. E. et al. Extracellular signal-related kinase positively regulates ataxia telangiectasia mutated, homologous recombination repair, and the DNA damage response. *Cancer Res.* **67**, 1046–1053 (2007).
67. Klomp, J. E. et al. CHK1 protects oncogenic KRAS-expressing cells from DNA damage and is a target for pancreatic cancer treatment. *Cell Rep.* **37**, 110060 (2021).
68. Pei, X. Y. et al. Cytokinetically quiescent (G0/G1) human multiple myeloma cells are susceptible to simultaneous inhibition of Chk1 and MEK1/2. *Blood* **118**, 5189–5200 (2011).
69. Stossel, C. et al. Spectrum of response to platinum and PARP inhibitors in germline BRCA-associated pancreatic cancer in the clinical and preclinical setting. *Cancer Discov.* **13**, 1826–1843 (2023).
70. Pusztai, L. et al. Durvalumab with olaparib and paclitaxel for high-risk HER2-negative stage II/III breast cancer: results from the adaptively randomized I-SPY2 trial. *Cancer Cell* **39**, 989–998.e5 (2021).

71. Hintzen, D. C. et al. The impact of monosomies, trisomies and segmental aneuploidies on chromosomal stability. *PLoS ONE* **17**, e0268579 (2022).
72. Holland, A. J. & Cleveland, D. W. Boveri revisited: chromosomal instability, aneuploidy and tumorigenesis. *Nat. Rev. Mol. Cell Biol.* **10**, 478–487 (2009).
73. Meena, J. K. et al. Telomerase abrogates aneuploidy-induced telomere replication stress, senescence and cell depletion. *EMBO J.* **34**, 1371–1384 (2015).
74. Andor, N. et al. Pan-cancer analysis of the extent and consequences of intratumor heterogeneity. *Nat. Med.* **22**, 105–113 (2016).
75. Smith, J. C. & Sheltzer, J. M. Genome-wide identification and analysis of prognostic features in human cancers. *Cell Rep.* **38**, 110569 (2022).
76. Moniz, L. S. & Stambolic, V. Nek10 Mediates G2/M cell cycle arrest and MEK autoactivation in response to UV irradiation. *Mol. Cell Biol.* **31**, 30–42 (2011).
77. Sun, C. et al. Rational combination therapy with PARP and MEK inhibitors capitalizes on therapeutic liabilities in RAS mutant cancers. *Sci. Transl. Med.* **9**, eaal5148 (2017).
78. Maertens, O. et al. MAPK pathway suppression unmasks latent DNA repair defects and confers a chemical synthetic vulnerability in BRAF-, NRAS-, and NF1-mutant melanomas. *Cancer Discov.* **9**, 526–545 (2019).
79. Russo, M. et al. Adaptive mutability of colorectal cancers in response to targeted therapies. *Science* **366**, 1473–1480 (2019).
80. Yuan, J., Dong, X., Yap, J. & Hu, J. The MAPK and AMPK signalings: interplay and implication in targeted cancer therapy. *J. Hematol. Oncol.* **13**, 1–19 (2020).
81. Darp, R., Vittoria, M. A., Ganem, N. J. & Ceol, C. J. Oncogenic BRAF induces whole-genome doubling through suppression of cytokinesis. *Nat. Commun.* **13**, 1–17 (2022).
82. Abulaiti, A., Fikaris, A. J., Tsygankova, O. M. & Meinkoth, J. L. Ras induces chromosome instability and abrogation of the DNA damage response. *Cancer Res.* **66**, 10505–10512 (2006).
83. Woo, R. A. & Poon, R. Y. C. Activated oncogenes promote and cooperate with chromosomal instability for neoplastic transformation. *Genes Dev.* **18**, 1317 (2004).
84. Luo, J. et al. A genome-wide RNAi screen identifies multiple synthetic lethal interactions with the ras oncogene. *Cell* **137**, 835–848 (2009).
85. Sanclemente, M. et al. c-RAF ablation induces regression of advanced Kras/Trp53 mutant lung adenocarcinomas by a mechanism independent of MAPK signaling. *Cancer Cell* **33**, 217–228.e4 (2018).
86. Sanclemente, M. et al. RAF1 kinase activity is dispensable for KRAS/p53 mutant lung tumor progression. *Cancer Cell* **39**, 294–296 (2021).
87. Ehrenreiter, K. et al. Raf-1 regulates Rho signaling and cell migration. *J. Cell Biol.* **168**, 955–964 (2005).
88. O'Neill, E., Rushworth, L., Baccarini, M. & Kolch, W. Role of the kinase MST2 in suppression of apoptosis by the proto-oncogene product Raf-1. *Science* **306**, 2267–2270 (2004).
89. Alavi, A. S., Acevedo, L., Min, W. & Cheresch, D. A. Chemoresistance of endothelial cells induced by basic fibroblast growth factor depends on Raf-1-mediated inhibition of the proapoptotic kinase, ASK1. *Cancer Res.* **67**, 2766–2772 (2007).
90. Eves, E. M. et al. Raf kinase inhibitory protein regulates aurora B kinase and the spindle checkpoint. *Mol. Cell* **23**, 561–574 (2006).
91. Mielgo, A. et al. A MEK-independent role for CRAF in mitosis and tumor progression. *Nat. Med.* **17**, 1641–1645 (2011).
92. Li, M. et al. The ATM-p53 pathway suppresses aneuploidy-induced tumorigenesis. *Proc. Natl. Acad. Sci. USA.* **107**, 14188–14193 (2010).
93. Crasta, K. et al. DNA breaks and chromosome pulverization from errors in mitosis. *Nature* **482**, 53–58 (2012).
94. Hatch, E. M., Fischer, A. H., Deerinck, T. J. & Hetzer, M. W. Catastrophic nuclear envelope collapse in cancer cell micronuclei. *Cell* **154**, 47 (2013).
95. Torres, E. M., Williams, B. R. & Amon, A. Aneuploidy: Cells losing their balance. *Genetics* **179**, 737–746 (2008).
96. Muenzner, J. et al. The natural diversity of the yeast proteome reveals chromosome-wide dosage compensation in aneuploids. *bioRxiv* <https://doi.org/10.1101/2022.04.06.487392> (2022).
97. Chen, J. et al. Cell cycle checkpoints cooperate to suppress DNA- and RNA-associated molecular pattern recognition and anti-tumor immune responses. *Cell Rep.* **32**, 108080 (2020).
98. Bakhom, S. F. et al. Chromosomal instability drives metastasis through a cytosolic DNA response. *Nature* **553**, 467–472 (2018).
99. Love, M. I., Huber, W. & Anders, S. Moderated estimation of fold change and dispersion for RNA-seq data with DESeq2. *Genome Biol.* **15**, 1–21 (2014).
100. Muller, H., Marzi, M. J. & Nicassio, F. IsomiRage: From functional classification to differential expression of miRNA isoforms. *Front. Bioeng. Biotechnol.* **2**, 38 (2014).
101. Demichev, V., Messner, C. B., Vernardis, S. I., Lilley, K. S. & Ralser, M. DIA-NN: neural networks and interference correction enable deep proteome coverage in high throughput. *Nat. Methods* **17**, 41–44 (2020).
102. Bateman, A. et al. UniProt: the universal protein knowledgebase in 2021. *Nucleic Acids Res.* **49**, D480–D489 (2021).
103. Meyers, R. M. et al. Computational correction of copy number effect improves specificity of CRISPR-Cas9 essentiality screens in cancer cells. *Nat. Genet.* **49**, 1779–1784 (2017).
104. Liberzon, A. et al. The molecular signatures database (MSigDB) hallmark gene set collection. *Cell Syst.* **1**, 417 (2015).
105. Colaprico, A. et al. TCGAbiolinks: an R/bioconductor package for integrative analysis of TCGA data. *Nucleic Acids Res.* **44**, e71 (2016).
106. Ritz, C., Baty, F., Streibig, J. C. & Gerhard, D. Dose-response analysis using R. *PLoS ONE* **10**, e0146021 (2015).
107. Fang, Z., Liu, X. & Peltz, G. GSEAPy: a comprehensive package for performing gene set enrichment analysis in Python. *Bioinformatics* **39**, btac757 (2023).
108. Talevich, E., Shain, A. H., Botton, T. & Bastian, B. C. CNVkit: Genome-wide copy number detection and visualization from targeted DNA sequencing. *PLoS Comput. Biol.* **12**, e1004873 (2016).
109. Bollen, S., Leddin, M., Andrade-Navarro, M. A. & Mah, N. CAFE: an R package for the detection of gross chromosomal abnormalities from gene expression microarray data. *Bioinformatics* **30**, 1484–1485 (2014).
110. Spurr, L. F. et al. Quantification of aneuploidy in targeted sequencing data using ASCETS. *Bioinformatics* **37**, 2461–2463 (2021).

## Acknowledgements

The authors would like to thank James McFarland for bioinformatic support; Gil Ast, Marina Mapelli, Zuzana Tothova and members of the Ben-David and Santaguida labs for helpful discussions; Varda Wexler for assistance with Figure preparation; Zuzana Storchova for providing the RPE1/RPT cell lines; René Medema and Jonne Raaijmakers for kindly providing the RPE1 monosomic clones (C1-C2-WA1-WA2-WA3); Ottavio Croci and Matteo Marzi for assistance with miRNA profiling; Agathe Niewienda and Daniela Ludwig for assistance with the proteomics acquisition; Nicholas Lyons, Jordan Bryan, Samantha Bender and Jennifer Roth for their assistance with the PRISM screen; Kevin Langley and the PhaseFocus team for their assistance with the LiveCyte® Analysis software; Jiyang Yu and Xiang Chen for providing the copy number data of the pediatric PDX cohort (EGAS00001002528). We thank the Broad

Institute Genomic Perturbation Platform for their assistance with the CRISPR/Cas9 screens, and the Center for the Development of Therapeutics and Repurposing Hub at the Broad Institute for providing the compound library. This work was supported by the European Research Council Starting Grant (grant #945674 to U.B.-D.) and Synergy grant (ERC-SyG-2020 951475 to M.R.), the Israel Cancer Research Fund Geshar Award (U.B.-D.), the Azrieli Foundation Faculty Fellowship (U.B.-D.), the DoD CDMRP Career Development Award (grant #CA191148 to U.B.-D.), the Israel Science Foundation (grant #1805/21 to U.B.-D.), the BSF project grant (grant #2019228 to U.B.-D.), the Forbeck Foundation (U.B.-D.), the Italian Association for Cancer Research (AIRC-MFAG 2018 - ID. 21665 and Bridge Grant 2023 - ID. 29228 projects to S.S.), Ricerca Finalizzata (GR-2018-12367077 to S.S.), Fondazione Cariplo (S.S.), the Rita-Levi Montalcini program from MIUR (to S.S.) and the Italian Ministry of Health with Ricerca Corrente and 5×1000 funds (S.S.), as well as the Ministry of Education and Research (BMBF), as part of the National Research Node 'Mass spectrometry in Systems Medicine (MSCoresys, O31LO220), the Deutsche Forschungsgemeinschaft (DFG, German Research Foundation, 492697668 to M.M). U.B.-D. is an EMBO Young Investigator. J.Z. was supported by a fellowship of the Israeli Ministry for Immigrant Absorption and by travel awards from the TAU Constantiner Institute and Cancer Biology Research Center. M.R.I. is supported by an AIRC Fellowship (ID 26738-2021). J.Z, Y.E, and G.L. are PhD and MD-PhD students within the graduate school of the Faculty of Medicine, Tel Aviv University. M.R.I., S.M, S.V. and S.S. are PhD students within the European School of Molecular Medicine (SEMM). Figure 6 was created using BioRender, released under a Creative Commons Attribution-NonCommercial-NoDerivs 4.0 International license.

## Author contributions

U.B.-D. and S.S. jointly conceived the study, directed and supervised it. J.Z. and M.R.I. jointly designed and performed most of the experiments. J.Z., M.R.I., U.B.-D. and S.S. analyzed the data with inputs from all co-authors. Y.E., E.R., J.M., E.C., E.S. and T.C. assisted with bioinformatic analyses. G.D.F., A.S.K., S.M, S.V., K.L., Y.C.-S., S.T., A.R. and S.S. assisted with in vitro experiments. G.L. generated aneuploidy scores. C.R. performed the miRNA profiling; J.M. and M.M. performed the proteomics; J.B. performed the primary drug screen. C.S. and T.G. performed the RNAseq of the pancreatic PDX tumors. F.N., E.R. and M.R. supervised the profilings and bioinformatic analyses performed in their labs. F.V. directed the genomic profiling and CRISPR screens. J.Z., M.R.I., U.B.-D. and S.S. wrote the manuscript with inputs from all co-authors.

## Competing interests

U.B.-D. received grant funding from Novocure, and receives consulting fees from Accent Therapeutics. E.Ruppin is a co-founder of MedAware,

Meabomed and Pangea Biomed (divested), and an unpaid member of Pangea Biomed's scientific advisory board. F.V. receives research support from the Dependency Map Consortium, Riva Therapeutics, Bristol Myers Squibb, Merck, Illumina, and Deerfield Management. F.V. is on the scientific advisory board of GSK, is a consultant and holds equity in Riva Therapeutics and is a co-founder and holds equity in Jumble Therapeutics. The other authors declare no competing interests.

## Additional information

**Supplementary information** The online version contains supplementary material available at <https://doi.org/10.1038/s41467-024-52176-x>.

**Correspondence** and requests for materials should be addressed to Uri Ben-David or Stefano Santaguida.

**Peer review information** *Nature Communications* thanks the anonymous reviewers for their contribution to the peer review of this work. A peer review file is available.

**Reprints and permissions information** is available at <http://www.nature.com/reprints>

**Publisher's note** Springer Nature remains neutral with regard to jurisdictional claims in published maps and institutional affiliations.

**Open Access** This article is licensed under a Creative Commons Attribution-NonCommercial-NoDerivatives 4.0 International License, which permits any non-commercial use, sharing, distribution and reproduction in any medium or format, as long as you give appropriate credit to the original author(s) and the source, provide a link to the Creative Commons licence, and indicate if you modified the licensed material. You do not have permission under this licence to share adapted material derived from this article or parts of it. The images or other third party material in this article are included in the article's Creative Commons licence, unless indicated otherwise in a credit line to the material. If material is not included in the article's Creative Commons licence and your intended use is not permitted by statutory regulation or exceeds the permitted use, you will need to obtain permission directly from the copyright holder. To view a copy of this licence, visit <http://creativecommons.org/licenses/by-nc-nd/4.0/>.

© The Author(s) 2024

<sup>1</sup>Department of Human Molecular Genetics and Biochemistry, Faculty of Medicine, Tel Aviv University, Tel Aviv, Israel. <sup>2</sup>Department of Experimental Oncology at IEO, European Institute of Oncology IRCCS, Milan, Italy. <sup>3</sup>Broad Institute of MIT and Harvard, Cambridge, MA, USA. <sup>4</sup>Charité Universitätsmedizin Berlin, Department of Biochemistry, Berlin, Germany. <sup>5</sup>Charité Universitätsmedizin Berlin, Core Facility High-Throughput Mass Spectrometry, Berlin, Germany. <sup>6</sup>Cancer Data Science Laboratory, Center for Cancer Research, National Cancer Institute, National Institutes of Health, Bethesda, MD, USA. <sup>7</sup>Center for Genomic Science of IIT@SEMM, Fondazione Istituto Italiano di Tecnologia, Milan, Italy. <sup>8</sup>Oncology Institute, Sheba Medical Center, Tel Hashomer, Israel. <sup>9</sup>Faculty of Medicine, Tel Aviv University, Tel Aviv, Israel. <sup>10</sup>Nuffield Department of Medicine, University of Oxford, Oxford, United Kingdom. <sup>11</sup>Max Planck Institute for Molecular Genetics, Berlin, Germany. <sup>12</sup>Department of Oncology and Hemato-Oncology, University of Milan, Milan, Italy. <sup>13</sup>These authors contributed equally: Johanna Zerbib, Marica Rosaria Ippolito. <sup>14</sup>These authors jointly supervised this work: Uri Ben-David, Stefano Santaguida.

✉ e-mail: [ubendavid@tauex.tau.ac.il](mailto:ubendavid@tauex.tau.ac.il); [Stefano.santaguida@ieo.it](mailto:Stefano.santaguida@ieo.it)